INTERNATIONAL JOURNAL FOR NUMERICAL METHODS IN ENGINEERING
Int. J. Numer. Meth. Engng 2016; **108**:790–816
Published online 18 March 2016 in Wiley Online Library (wileyonlinelibrary.com). DOI: 10.1002/nme.5243

An efficient and high-order frequency-domain approach for transient acoustic–structure interactions in three dimensions

Junshan Lin*,†

Department of Mathematics and Statistics, Auburn University, Auburn, AL 36849, USA

SUMMARY

This paper is concerned with numerical solution of the transient acoustic–structure interaction problems in three dimensions. An efficient and higher-order method is proposed with a combination of the exponential window technique and a fast and accurate boundary integral equation solver in the frequency-domain. The exponential window applied to the acoustic–structure system yields an artificial damping to the system, which eliminates the wrap-around errors brought by the discrete Fourier transform. The frequency-domain boundary integral equation approach relies on accurate evaluations of relevant singular integrals and fast computation of nonsingular integrals via the method of equivalent source representations and the fast Fourier transform. Numerical studies are presented to demonstrate the accuracy and efficiency of the method.

Received 10 November 2015; Revised 19 February 2016; Accepted 19 February 2016

KEY WORDS: acoustic–structure interaction; frequency-domain approach; exponential window; boundary integral equation

1. INTRODUCTION

The dynamic interaction between a structure and surrounding compressible, inviscid fluid medium is encountered in many areas of engineering and industrial design and identification, such as detection of submerged objects, vibration analysis for aircrafts and automobiles, and ultrasound vibro-acoustography [1–4]. The problem could be acoustic radiation from a mechanically excited elastic structure or acoustic scattering from a submerged elastic structure. Accurate numerical solution for the dynamic response of such coupled systems in three dimensions poses significant challenges because of the highly oscillatory nature of the wave fields and the infinite fluid domain under consideration.

The vast majority of the research has been devoted to the acoustic–structure interactions in the frequency-domain. We refer the readers to [5, 6] for theoretical investigations and [7–23] and the reference therein for the related numerical studies. Several advanced numerical simulators have been developed to model the transient structural acoustics. These include the time-domain finite element methods (FEMs) and spectral element methods (e.g., [24–28]). Both methods involve spatial discretization over the three-dimensional structure and fluid domains. Moreover, the infinite fluid domain has to be truncated into a finite one by imposing certain artificial boundary conditions, such as the absorbing boundary condition [29] or the perfectly matched layer [30]. In general, the boundary condition has to be prescribed sufficiently far away from the structure to reduce the reflection of acoustic waves from the absorbing boundary. The accuracy of the time-domain perfectly matched layer method, on the other hand, has not been fully investigated for complex dynamic systems [31, 32]. Another type of approach is based on the FEM–boundary element method framework,

*Correspondence to: Department of Mathematics and Statistics, Auburn University, Auburn, AL 36849, USA.
†E-mail: jzl0097@auburn.edu.

wherein the time-domain boundary element method is applied to model the acoustic wave propagation in the fluid and FEM is used to model the elastic waves in the structure [33, 34]. The method offers some advantages from a numerical perspective because the modeling of the acoustic wave only involves discretization on the structure-acoustic interface and the radiation condition at the infinity is enforced automatically in the integral formulations. However, the time-stepping procedure may experience instability issues, and an adequate choice of the time step size has to be chosen [35].

In this paper, we develop an accurate and stable frequency-domain approach for the transient acoustic–structure interactions in three dimensions. The standard frequency-domain approach for transient analysis amounts to solving the problem at a series of real sampling frequencies and then transforming the solutions at discretized frequencies back to the time domain via the discretized Fourier transform (DFT). The periodic nature of the DFT requires that the initial and ending responses match within one time period. Otherwise, the so-called wrap-around errors will occur. This is usually achieved by adding a duration of trailing zeroes at the end of the force history to allow the free vibration to damp out, and the system becomes quiescent at the end of the time period. For an acoustic–structure dynamic system with multiple reflections of waves and low dissipation, the duration has to be long. This is computationally expensive because of the extremely large time period needed for the implementation of the DFT and, consequently, a large number of sampling frequencies over the frequency-domain. Here, we employ an exponential window method to add an artificial damping to the system so that the vibration will damp out quickly and a long duration for trailing zeroes is not necessary. As a result, the number of sampling frequencies is significantly reduced.

In order to obtain the solution for the acoustic–structure interaction problem at each single sampling frequency in an efficient and accurate manner, a fast and high-order boundary integral equation solver is introduced through accelerated computation of nonsingular integrals and accurate evaluation of singular integrals. The method has its independent interest for modeling the acoustic–structure interactions in the frequency-domain. It computes one matrix-vector product associated with the discretization of the integral equations with $O\left(N_\Gamma^{4/3}\log N_\Gamma\right)$ operations, wherein N_Γ is the number of the surface discretization points. Compared with a brute-force integration scheme with $O\left(N_\Gamma^2\right)$ computation cost for each matrix-vector product, the computation of integrals by the proposed algorithm is significantly accelerated, in particular for the sampling at medium and high frequencies, for which N_Γ has to be large to resolve the wave fields with sufficient accuracy. The method also exhibits algebraic convergence and attains the accuracy of traditional boundary element methods. Furthermore, the sampling of solutions for the frequency-domain problems at discrete frequencies is independent and is implemented naturally in parallel. We point out that there exist other numerical algorithms to evaluate the discretized integral equations in a fast way, such as the fast multipole method [36–38]. The method offers significant gains in computation time with $O(N_\Gamma \log N_\Gamma)$ operations only. However, fast multipole method seems to present low-order accuracy for wave scattering (e.g., [39, 40]). In addition, multiple-tree frames are needed because of the co-existence of longitudinal and transverse waves in the elastic structure, which results in a nonuniform definition for well-separated groups and greatly complicates the implementation [41].

The rest of the paper is organized as follows. Section 2 introduces the mathematical model for the acoustic–structure interaction. The exponential window method and the main algorithm for the transient analysis are presented in Section 3. Section 4 is devoted to the boundary integral equation method in the frequency-domain, where accurate evaluation of singular integrals and acceleration for nonsingular integrations are discussed in details. We show various numerical results in Section 5 to demonstrate the accuracy and efficiency of the method and conclude with some remarks in Section 6.

2. PROBLEM FORMULATION

We consider the configuration wherein an elastic solid is submerged in an infinite acoustic fluid medium. The excitation force can be generated in the interior of the solid domain (*radiation problem*) or in the exterior of the fluid domain (*scattering problem*) as shown in Figure 1. Let $\Omega \subset \mathbb{R}^3$

DOI: 10.1002/nme

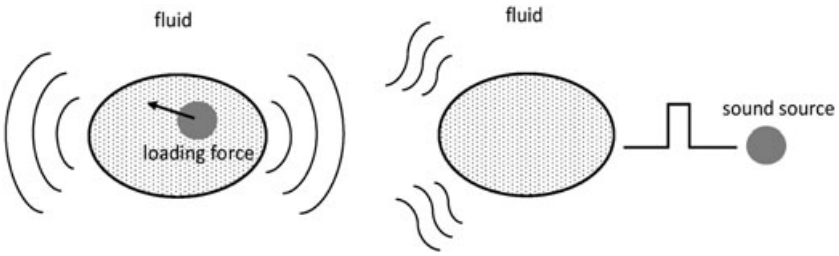

Figure 1. Problem geometry: an elastic structure submerged in the fluid medium. Left: radiation problem where the force is generated inside the structure. Right: scattering problem where the acoustic source is excited in the fluid medium.

be the domain of the elastic structure and $\Omega^c = \mathbb{R}^3 \backslash \bar{\Omega}$ be the exterior acoustic fluid region. The elastic body is homogeneous and isotropic with the corresponding Lamé constants λ and μ and the density ρ_e. Let $\mathbf{u}(x,t)$ be the displacement and $\boldsymbol{\varepsilon}(x,t)$ be the strain tensor defined by

$$\boldsymbol{\varepsilon} = \frac{1}{2}\left(\nabla \mathbf{u} + \nabla \mathbf{u}^T\right).$$

Then the Cauchy stress tensor $\boldsymbol{\sigma}(x,t)$ is given by the Hook's law:

$$\sigma_{ij} = \lambda \sum_{k=1}^{3} \varepsilon_{kk} + 2\mu \varepsilon_{ij}, \quad i,j = 1,2,3.$$

The elastodynamics in the structure is described by the Navier equation

$$\rho_e \frac{\partial^2 \mathbf{u}}{\partial t^2} = \nabla \cdot \boldsymbol{\sigma} + \mathbf{f} \quad \text{in } \Omega \times (0,T),$$

where $(0,T)$ is the time interval and $\mathbf{f}$ is the loading force generated inside the structure in the case of radiation problem. For the scattering problem when an acoustic wave impinges on the structure from the exterior, we have $\mathbf{f} = 0$. Equivalently, the displacement vector $\mathbf{u}$ is governed by the following elastic wave equation:

$$\rho_e \frac{\partial^2 \mathbf{u}}{\partial t^2} = (\lambda + 2\mu)\, \nabla\nabla \cdot \mathbf{u} - \mu\, \nabla \times \nabla \times \mathbf{u} + \mathbf{f} \quad \text{in } \Omega \times (0,T). \tag{2.1}$$

Let ρ_f and c_f be the density and wave speed in the acoustic fluid medium, respectively. Then the pressure field $p(x,t)$ in the acoustic medium satisfies the following scalar wave equation:

$$\frac{1}{c_f^2} \frac{\partial^2 p}{\partial t^2} - \Delta p = g \quad \text{in } \Omega^c \times (0,T), \tag{2.2}$$

where g is the acoustic excitation source in the case of scattering problem. It is assumed that g vanishes outside a bounded domain $D \subset \Omega^c$. In the radiation problem when the structure is mechanically excited in the interior, we have $g = 0$.

To couple two media, the equilibrium of the force and the compatibility of the normal displacement are imposed on the fluid–solid interface Γ. More precisely,

$$\boldsymbol{\sigma} \cdot \mathbf{n} = -p\, \mathbf{n}, \quad \frac{\partial p}{\partial n} = -\rho_f \frac{\partial^2 \mathbf{u}}{\partial t^2} \cdot \mathbf{n} \quad \text{for } \Gamma \times (0,T). \tag{2.3}$$

The system is assumed to be quiescent at the beginning, and the following homogeneous initial conditions are prescribed:

$$\mathbf{u}(x,0) = \frac{\partial \mathbf{u}(x,0)}{\partial t} = \mathbf{0} \quad \text{for } x \in \Omega \tag{2.4}$$

DOI: 10.1002/nme

and

$$p(x,0) = \frac{\partial p(x,0)}{\partial t} = 0 \quad \text{for } x \in \Omega^c. \tag{2.5}$$

3. FREQUENCY-DOMAIN APPROACH FOR THE TRANSIENT ANALYSIS AND THE EXPONENTIAL WINDOW METHOD

Let T be the time period of the transient response and N_ω be the number of sampling points. One has the time resolution $\Delta t = T/N_\omega$ and the frequency resolution $\Delta\omega = 2\pi/T$. In the frequency-domain approach, the quantities of interests ($\mathbf{u}$ or p) are obtained at a series of sampling frequencies ω_n ($n = 0, 1, \ldots, N_\omega - 1$) and then transformed back into the time domain using the DFT. The Nyquist frequency is given by $N_\omega \Delta\omega/4\pi$, and N_ω is chosen such that responses corresponding to higher frequencies are insignificant.

In the implementation of the frequency-domain approach, a quiet zone of trailing zeroes has to be added at the end of the force history in order to circumvent the wrap-around errors brought by the DFT. In general, the duration of this zone must be sufficiently long to allow the free vibration to damp out, and the system becomes quiescent at the end of the time period. In a low dissipative acoustic–structure dynamic system, the free-vibration will decay slowly because of multiple scattering and reflections of the waves. Therefore, the standard application of the DFT would require extremely long duration of the trailing zeroes, or equivalently large time period T, which gives rise to highly expensive computational cost. Here, we employ the exponential window method to add an artificial damping to the system. This is achieved by introducing a damping factor $e^{-\eta t}$ to the displacement vector $\mathbf{u}(x,t)$ and the pressure field $p(x,t)$ so that both will achieve desirable tolerance at the end of the time period T for some $\eta > 0$. The technique has been applied to signal processing and recently to structural dynamics [42–44].

Let us introduce the damped quantities

$$\mathbf{u}_d(x,t) = e^{-\eta t}\mathbf{u}(x,t) \quad \text{and} \quad p_d(x,t) = e^{-\eta t}p(x,t).$$

Define the Fourier transforms of $\mathbf{u}_d$ and p_d as

$$\widehat{\mathbf{u}_d}(x,\omega) := \frac{1}{2\pi}\int_{-\infty}^{+\infty} \mathbf{u}_d(x,t)e^{i\omega t}\,\mathrm{d}t \quad \text{and} \quad \widehat{p_d}(x,\omega) := \frac{1}{2\pi}\int_{-\infty}^{+\infty} p_d(x,t)e^{i\omega t}\,\mathrm{d}t$$

and the associated inverse Fourier transforms as

$$(\widehat{\mathbf{u}_d})^\vee(x,t) := \int_{-\infty}^{+\infty} \widehat{\mathbf{u}_d}(x,\omega)e^{-i\omega t}\,\mathrm{d}\omega \quad \text{and} \quad (\widehat{p_d})^\vee(x,t) := \int_{-\infty}^{+\infty} \widehat{p_d}(x,\omega)e^{-i\omega t}\,\mathrm{d}\omega.$$

It is observed that

$$\widehat{\mathbf{u}_d}(x,\omega) = \hat{\mathbf{u}}(x,\omega + i\eta) \quad \text{and} \quad \widehat{p_d}(x,\omega) = \hat{p}(x,\omega + i\eta), \tag{3.1}$$

where $\hat{\mathbf{u}}$ and $\hat{p}$ are Fourier transforms of $\mathbf{u}$ and p, respectively. Note that the poles of $\hat{\mathbf{u}}(\cdot,\omega)$ and $\hat{p}(\cdot,\omega)$ lie on the lower complex ω-plane (cf. [6]); thus, the aforementioned Fourier transforms are well defined.

Instead of computing $u(x,t)$ and $p(x,t)$ directly, we first apply the frequency-domain approach to obtain $\mathbf{u}_d(x,t)$ and $p_d(x,t)$, which are damped out at the end of the period with the use of the damping factor $e^{-\eta t}$. In light of (3.1), the computation of $\widehat{\mathbf{u}_d}$ and $\widehat{p_d}$ at the discrete frequencies $n\Delta\omega$ is equivalent to the sampling of $\hat{\mathbf{u}}$ and $\hat{p}$ at complex frequencies $\omega_n = n\Delta\omega + i\eta$ ($n = 0, 1, \ldots, N_\omega - 1$). That is, we solve the following coupled PDEs at complex frequencies $\omega = n\Delta\omega + i\eta$:

$$(\lambda + 2\mu)\,\nabla\nabla\cdot\hat{\mathbf{u}} - \mu\,\nabla\times\nabla\times\hat{\mathbf{u}} + \rho_e\omega^2\hat{\mathbf{u}} = -\hat{\mathbf{f}} \quad \text{in} \quad \Omega; \tag{3.2}$$

DOI: 10.1002/nme

$$\Delta \hat{p} + \kappa_f^2 \hat{p} = -\hat{g} \quad \text{in} \quad \Omega^c. \tag{3.3}$$

$$\hat{\boldsymbol{\sigma}} \cdot \mathbf{n} = -\hat{p}\, \mathbf{n}, \quad \frac{\partial \hat{p}}{\partial n} = \rho_f \omega^2 \hat{\mathbf{u}} \cdot \mathbf{n} \quad \text{on} \quad \Gamma. \tag{3.4}$$

$$\lim_{r\to\infty} r \left(\frac{\partial \hat{p}}{\partial r} - i\kappa_f \hat{p} \right) = 0, \quad r = |x|. \tag{3.5}$$

Here, $\kappa_f = \omega/c_f$ denotes the wave number in the acoustic medium, and (3.5) is the so-called Sommerfeld radiation condition at infinity [6]. By taking the inverse DFT, the damped signals $\mathbf{u}_d$ and p_d can be obtained in the time domain. The original displacement vector and the pressure field are then recovered by

$$\mathbf{u}(x,t) = e^{\eta t}\mathbf{u}_d(x,t) \quad \text{and} \quad p(x,t) = e^{\eta t} p_d(x,t). \tag{3.6}$$

Therefore, with the exponential window method, our frequency-domain approach for the transient analysis of acoustic–structure interactions can be described as follows:

(1) Perform DFT for the damped loading function $\mathbf{f}_d(x,t) = e^{-\eta t}\mathbf{f}(x,t)$ or the damped acoustic source function $g_d(x,t) = e^{-\eta t} g(x,t)$ to obtain the frequency-domain loading force or acoustic source for $n = 0, 1, \ldots, N_\omega - 1$:

$$\widehat{\mathbf{f}_d}(x, n\Delta\omega) = \frac{1}{N_\omega} \sum_{k=0}^{N_\omega - 1} \mathbf{f}_d(x,t_k) e^{i2\pi kn/N_\omega}, \quad \widehat{g_d}(x, n\Delta\omega) = \frac{1}{N_\omega} \sum_{k=0}^{N_\omega - 1} g_d(x,t_k) e^{i2\pi kn/N_\omega}.$$

(2) Sample $\hat{\mathbf{u}}$ and $\hat{p}$ for the first $N_\omega/2 + 1$ complex frequencies by solving (3.2)–(3.5) at $\omega_n = n\Delta\omega + i\eta$ $(n = 0, 1, \ldots, N_\omega/2)$, wherein the sources terms are given by $\hat{\mathbf{f}}(x,\omega_n) = \widehat{\mathbf{f}_d}(x, n\Delta\omega)$ and $\hat{g}(\omega_n) = \widehat{g_d}(x, n\Delta\omega)$. Let

$$\widehat{\mathbf{u}_d}(x, n\Delta\omega) = \hat{\mathbf{u}}(x,\omega_n) \quad \text{and} \quad \widehat{p_d}(x, n\Delta\omega) = \hat{p}(x,\omega_n).$$

(3) Evaluate $\widehat{\mathbf{u}_d}$ and $\widehat{p}_d$ for the last $N_\omega/2 - 1$ frequencies by performing the complex conjugate. That is,

$$\widehat{\mathbf{u}_d}(x, n\Delta\omega) = \overline{\widehat{\mathbf{u}_d}(x, (N_\omega - n)\Delta\omega)} \quad \text{and} \quad \widehat{p_d}(x, n\Delta\omega) = \overline{\widehat{p_d}(x, (N_\omega - n)\Delta\omega))}$$

$$\text{for } n = N_\omega/2 + 1, N_\omega/2 + 2, \ldots, N_\omega - 1.$$

(3) Perform the inverse DFT to obtain the damped signals in the time domain:

$$\mathbf{u}_d(x, n\Delta t) = \sum_{k=0}^{N_\omega - 1} \widehat{\mathbf{u}_d}(x, k\Delta\omega) e^{-i2\pi kn/N_\omega} \quad \text{and} \quad p_d(x, n\Delta t) = \sum_{k=0}^{N_\omega - 1} \widehat{p_d}(x, k\Delta\omega) e^{-i2\pi kn/N_\omega},$$

$$n = 0, 1, \ldots, N_\omega - 1.$$

(4) Recover the original wave fields in the time window $[0, T]$ using $\mathbf{u}(x,t) = e^{\eta t}\mathbf{u}_d(x,t)$ and $p(x,t) = e^{\eta t} p_d(x,t)$.

In the algorithm, the damping parameter is chosen such that $e^{\eta T} = 10^m$ for some positive integer m. That is, the signal is damped by a factor of 10^{-m} at the end of the time period. Because the factor $e^{\eta t}$, on the other hand, amplifies the numerical errors arising from the solution of the frequency-domain problem when performing the recovery of $\mathbf{u}(x,t)$ and $p(x,t)$ through the formula (3.6), m cannot be arbitrarily large. To address this issue, we expand the time window to $[0, \tilde{m}T]$ in the numerical calculation for some positive integer $\tilde{m}$. Then if the signal is damped by a factor of 10^{-m}

DOI: 10.1002/nme

at the end of the new time period, there will be a loss of precision with an order of $10^{m/\tilde{m}}$ when performing step (4) in the time window of interest, $[0, T]$. For a given tolerance ϵ, the integers m and $\tilde{m}$ may be chosen by following the two principles: (i) the signal is damped out at the end of the period such that $|\mathbf{u}_d(x, \tilde{m}T)| < \epsilon$, $|p_d(x, \tilde{m}T)| < \epsilon$, and (ii) the loss of precision in performing step (4) is within a desirable tolerance such that high-order accuracy is retained for the time-domain solution. To achieve the latter, we set $\tilde{m} = m$; thus, when a second-order accuracy scheme is applied to solve (3.2)–(3.5) with three-digit accuracy, it can be guaranteed that two-digit accuracy is achieved for the time-domain solution in $[0, T]$. From the numerical experiments, it is also observed that $m = 2$ is usually sufficient to damp out the free vibration.

It is seen that the main computational cost for the proposed approach arises in step (2) when solving the frequency-domain acoustic–structure interaction problem (3.2)–(3.5) at $N_\omega/2 + 1$ sampling frequencies. For each fixed frequency $\omega = \omega_n$, we propose a fast and accurate boundary integral equation method to obtain the physical quantities of $\hat{\mathbf{u}}(x, \omega_n)$ and $\hat{p}(x, \omega_n)$. This is discussed in details in the next section. It is also noted that solving for the problem (3.2)–(3.5) at discrete frequencies is independent and can be implemented in parallel.

4. FAST AND ACCURATE BOUNDARY INTEGRAL EQUATION METHOD FOR THE FREQUENCY-DOMAIN ACOUSTIC–STRUCTURE INTERACTION PROBLEM

To solve (3.2)–(3.5) via the boundary integral equation approach, a partition of unity and a semi-classical method are employed to evaluate singular integrals accurately. Nonsingular integrals are computed by high-order quadrature rules with an accelerated scheme, wherein each matrix-vector product requires $O\left(N_\Gamma^{4/3} \log N_\Gamma\right)$ operations. The acceleration strategy relies on the two-face equivalent source approximation, which reduces the evaluation of non-adjacent interactions in the integral formulations to an evaluation of three-dimensional fast Fourier transform (FFT). The method was first applied to the acoustic wave scattering in [45] and then to the elastic scattering in [46]. Here, we extend the method to the acoustic–structure interaction problem.

4.1. Boundary integral equations

Let $G(\kappa; x, y) = \frac{e^{i\kappa|x-y|}}{4\pi|x-y|}$ be the Green's function for the Helmholtz equation $\Delta\varphi + \kappa^2\varphi = 0$ in $\mathbb{R}^3$ and $\mathbb{G}(x, y)$ be the dyadic Green function for the elastic wave equation that satisfies

$$(\lambda + 2\mu)\, \nabla\nabla \cdot \mathbb{G}(x, y) - \mu\, \nabla \times \nabla \times \mathbb{G}(x, y) + \rho_e\omega^2\mathbb{G}(x, y) = -\delta(x - y)\mathbb{I}.$$

Then each component of $\mathbb{G}(x, y)$ is expressed as

$$g_{ij}(x, y) = \frac{1}{\rho_e\omega^2}\left[\delta_{ij}\kappa_s^2 G(k_s; x - y) + \frac{\partial}{\partial x_i}\frac{\partial}{\partial x_j}\left(G(\kappa_s; x, y) - G(\kappa_p; x - y)\right)\right],$$

where δ_{ij} is the Kronecker delta, $\kappa_p = \frac{\omega\sqrt{\rho_e}}{\sqrt{\lambda+2\mu}}$ and $\kappa_s = \frac{\omega\sqrt{\rho_e}}{\sqrt{\mu}}$ are wave numbers for the longitudinal wave (P-wave) and the transverse wave (S-wave), respectively.

Let $\bar{\bar{\gamma}}(x, y) = \gamma(\nabla_y \cdot \mathbb{G}(x, y))\mathbb{I} + \mu\left(\nabla_y\mathbb{G}(x, y) + \nabla_y\mathbb{G}^T(x, y)\right)$ be the third rank Green tensor [47]. Then the Green tensor for the traction at the interface Γ is given by $\mathbb{T}(x, y) = \bar{\bar{\gamma}}_i(x, y) \cdot \mathbf{n}(y)$, where $\mathbf{n}$ is the unit outward normal on Γ. By the Green's identity, the elastic displacement $\hat{\mathbf{u}}$ and the acoustic pressure $\hat{p}$ satisfy the following boundary integral equations, respectively:

$$\frac{1}{2}\hat{\mathbf{u}}(x) = \int_\Gamma \left[\mathbb{G}(x, y)\ (\hat{\boldsymbol{\sigma}} \cdot \mathbf{n}) - \mathbb{T}(x, y)\ \hat{\mathbf{u}}(y)\right] \mathrm{d}s_y + \int_\Omega \mathbb{G}(x, y)\ \hat{\mathbf{f}}(y)\mathrm{d}y \quad x \in \Gamma$$

and

$$\frac{1}{2}\hat{p}(x) = \int_\Gamma \left[\frac{\partial G}{\partial n}(\kappa_f; x, y)\ \hat{p}(y) - G(\kappa_f; x, y)\ \frac{\partial \hat{p}}{\partial n}(y)\right] \mathrm{d}s_y + \int_D G(\kappa_f; x, y)\ \hat{g}(y)\mathrm{d}y \quad x \in \Gamma.$$

DOI: 10.1002/nme

In light of the continuity conditions (3.4) along the interface, we arrive at the coupled system of integral equations defined over the interface Γ:

$$\frac{1}{2}\hat{\mathbf{u}}(x) - \int_\Gamma \left[\mathbb{G}(x,y)\left(-\hat{p}(y)\mathbf{n}(y)\right) - \mathbb{T}(x,y)\hat{\mathbf{u}}(y)\right] \mathrm{d}s_y = \int_\Omega \mathbb{G}(x,y)\,\hat{\mathbf{f}}(y)\mathrm{d}y; \tag{4.1}$$

$$\frac{1}{2}\hat{p}(x) - \int_\Gamma \left[\frac{\partial G}{\partial n}(x,y)\;\hat{p}(y) - G(x,y)\left(\rho_f \omega^2 \hat{\mathbf{u}}(y)\cdot\mathbf{n}(y)\right)\right] \mathrm{d}s_y = \int_D G(x,y)\;\hat{g}(y)\mathrm{d}y. \tag{4.2}$$

Here and henceforth, for conciseness, we omit the notation κ_f in the Green's function of the Helmholtz equation.

The unknown quantities in the aforementioned system are the displacement $\hat{\mathbf{u}}$ and the pressure field $\hat{p}$ on Γ. The integral equations are discretized, and an iterative method, such as generalized minimal residual (GMRES) [48], is applied to solve the associated linear system. To achieve a fast and high-order accuracy algorithm, accurate evaluation of singular integrals and fast computation of nonsingular integrals on the left side of (4.1) and (4.2) are performed for each matrix-vector product in the iterative method. This is elaborated in the rest of this section.

4.2. *Decomposition of the integrals*

4.2.1. Partition of unity over the interface. Let $x_1, x_2, \ldots, x_{N_\Gamma}$ be the surface discretization points over Γ. We first cover Γ by a set of overlapping patches $\{\mathcal{P}_m\}_{m=1}^M$, where each patch $\mathcal{P}_m$ is the image of an open set $\mathcal{H}_m \subset \mathbb{R}^2$ via a smooth invertible mapping Φ_m (Figure 2). A partition of unity subordinated to this covering is chosen such that

$$\sum_{m=1}^M w_m(x) = 1 \text{ and each } w_m(x) \text{ is smooth and vanishes outside the patch } \mathcal{P}_m.$$

The choices of w_m are not unique. For instance, they can be mollifier functions (cf. [49]) under suitable normalization to guarantee that the sum $\sum_{m=1}^M w_m(x) = 1$. Figure 3 demonstrates one example of such functions. It is also preferable that w_m has small derivatives such that dense sampling is not required to capture fast transition of the functions. With the overlapping patches and the associated partition of unity, each integration over the surface Γ in (4.1) and (4.2) may be reduced to evaluation of integrals for compactly supported functions:

$$\int_\Gamma \ldots \,\mathrm{d}s_y = \sum_{m=1}^M \int_{\mathcal{P}_m} \ldots \; w_m(y)\,\mathrm{d}s_y. \tag{4.3}$$

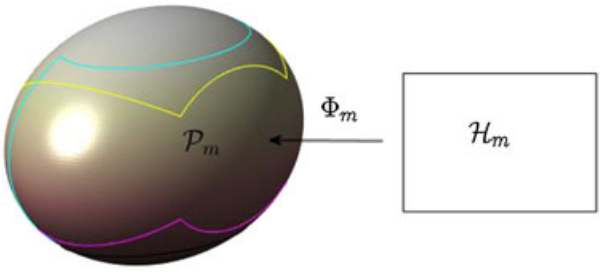

Figure 2. Overlapping patches $\{\mathcal{P}_m\}_{m=1}^M$ that cover the surface, wherein each patch $\mathcal{P}_m$ is the image of an open set $\mathcal{H}_m$ in $\mathbb{R}^2$.

DOI: 10.1002/nme

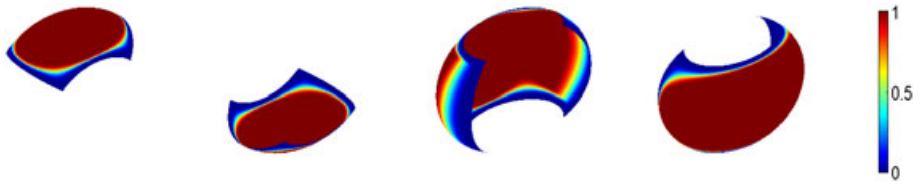

Figure 3. A partition of unity associated with a covering of the surface with four overlapping patches. The color over each patch denotes the value of w_m. Each $w_m(x)$ is given by normalization of a mollifier function, and their sum satisfies $\sum_{m=1}^{M} w_m(x) = 1$.

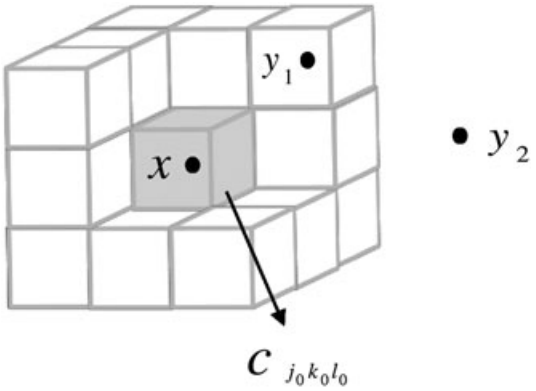

Figure 4. The adjacent set $\mathcal{A}_x$ contains 27 cubic cells: $c_{j_0k_0l_0}$ and its 26 neighboring cells. In the figure, x and y_1 are adjacent, while x and y_2 are non-adjacent.

4.2.2. Cubic cells and adjacency. To implement fast evaluation of nonsingular integrals, we introduce a large cubic cell $\mathcal{C}$ containing the elastic body Ω.[‡] The cubic $\mathcal{C}$ is decomposed into L^3 small identical cubic cells c_{jkl} $(j, k, l = 1, 2, \ldots, L)$ such that there are L cells along the x_1, x_2, and x_3 directions, respectively. It is noted that most cubic cells do not contain any surface points on Γ because the interface is a two-dimensional manifold. Indeed, the number of non-empty cells is approximately $O(L^2)$. Taking into account that there is a total of N_Γ points over Γ, each of those non-empty cells contains approximately $O\left(N_\Gamma/L^2\right)$ points.

To achieve desirable accuracy while reducing computational cost for the overall discretization, the evaluations of adjacent (singular) and non-adjacent (nonsingular) integrals are treated in different ways. To this end, we give the precise definition of adjacency as follows. For a surface discretization point x that lies in the interior of some cell $c_{j_0k_0l_0}$, let

$$\mathcal{A}_x := \{\, y \mid y \in c_{jkl}, |j - j_0| \leqslant 1, |k - k_0| \leqslant 1, |l - l_0| \leqslant 1\} \tag{4.4}$$

be the set containing the cell $c_{j_0k_0l_0}$ and its 26 neighboring cells (Figure 4). Then two points x and y are called adjacent if $y \in \mathcal{A}_x$ and non-adjacent if otherwise. If x sits on the face of two neighboring cells $c_{\bar{j}_0\bar{k}_0\bar{l}_0}$ and $c_{\tilde{j}_0\tilde{k}_0\tilde{l}_0}$, we set $j_0 = \min\left\{\bar{j}_0, \tilde{j}_0\right\}$, $k_0 = \min\left\{\bar{k}_0, \tilde{k}_0\right\}$, $l_0 = \min\left\{\bar{l}_0, \tilde{l}_0\right\}$ and define $\mathcal{A}_x$ as in (4.4).

4.2.3. Adjacent and non-adjacent interactions. The evaluation of the integral (4.3) on each patch can be decomposed as adjacent and non-adjacent interactions as follows:

$$\int_{\mathcal{P}_m} \ldots\, w_m(y)\, \mathrm{d}s_y = \int_{\mathcal{P}_m \cap \mathcal{A}_x} \ldots w_m(y)\, \mathrm{d}s_y + \int_{\mathcal{P}_m \cap \mathcal{A}_x^c} \ldots w_m(y)\, \mathrm{d}s_y, \tag{4.5}$$

[‡]For elongated elastic structure, a three-dimensional slab is preferable (see Example 3 in Section 5). Here, we limit our discussion to a cube for clarity of exposition.

DOI: 10.1002/nme

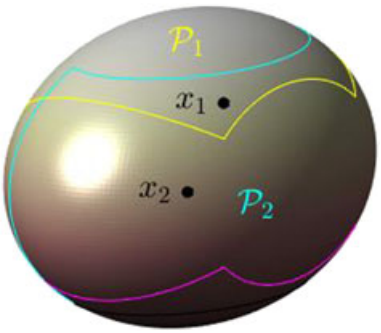

Figure 5. For x_1, the adjacent integrals over $\mathcal{P}_1$ and $\mathcal{P}_2$ are both singular, because x_1 lies in the region where two patches overlap. For x_2, the adjacent integral over $\mathcal{P}_1$ and $\mathcal{P}_2$ is nonsingular and singular, respectively. Because x_2 lies in $\mathcal{P}_2$, but not in $\mathcal{P}_1$.

where $\mathcal{A}_x^c$ denotes the complement of the adjacent set $\mathcal{A}_x$ in $\mathbb{R}^3$. Furthermore, we distinguish two types of adjacent interactions: the case when the patch $\mathcal{P}_m$ contains the target point x and the case when it does not. Obviously, the singularity occurs for the former and would require special evaluations of singular integrals, while the integral for the latter is nonsingular and the standard trapezoidal quadrature rule can still be applied. To this end, we define an index set, $\mathcal{I}_x := \{\, m \mid x \in \mathcal{P}_m\}$, that counts all the patches containing the target point x. If x belongs to a region where several patches overlap, then the set $\mathcal{I}_x$ has more than one element. Otherwise, $\mathcal{I}_x$ has only one element. Now, for a given target point x, the adjacent integral $\int_{\mathcal{P}_m \cap \mathcal{A}_x} \dots w_m(y)\, \mathrm{d}s_y$ over the patch $\mathcal{P}_m$ is a singular interaction if $m \in \mathcal{I}_x$ and a nonsingular interaction if $m \notin \mathcal{I}_x$. Figure 5 illustrates such two cases of adjacent interactions.

Therefore, in light of (4.3)–(4.5) and the definition of singular and nonsingular adjacent interactions, for a given target point x, the whole integral can be split into three separate parts:

$$\sum_{m \notin \mathcal{I}_x} \int_{\mathcal{P}_m \cap \mathcal{A}_x} \dots w_m(y)\, \mathrm{d}s_y \;+\; \sum_{m \in \mathcal{I}_x} \int_{\mathcal{P}_m \cap \mathcal{A}_x} \dots w_m(y)\, \mathrm{d}s_y \;+\; \sum_{m=1}^{M} \int_{\mathcal{P}_m \cap \mathcal{A}_x^c} \dots w_m(y)\, \mathrm{d}s_y. \tag{4.6}$$

The first part in the aforementioned decomposition is the adjacent nonsingular interactions. Note that the integrand vanishes to high order at the boundary of each patch because of the function $w_m(y)$ being used for the partition of unity. The trapezoidal rule would yield super-algebraic convergence for such an integrand. The computational cost arising from this part for all target points is $O\left(N_\Gamma^2/L^2\right)$, because $O\left(N_\Gamma/L^2\right)$ surface points lie inside each cubic cell. The second part of (4.6) is a singular integral. Similar to the first part, such adjacent interactions also require $O\left(N_\Gamma^2/L^2\right)$ operations. However, the integral kernel can be weakly or strongly singular; hence, accurate evaluations of those singular integrals over the surface are essential to guarantee a high-order scheme for the whole integration. The last part are non-adjacent nonsingular interactions, for which high-order accuracy can still be retained by the standard trapezoidal rule. However, a direct use of such an integrator would lead to an $O(N_\Gamma^2)$ computational cost, which becomes extremely expensive when N_Γ is large. In what follows, we discuss accurate evaluation of the second part and accelerated computation of the third part in (4.6).

4.3. Accurate singular integration

For each patch $\mathcal{P}_m$, the evaluation of singular integrals are carried out in the parameter space. We recall the notations in Section 4.2.1. The mapping $\Phi_m : \mathbb{R}^2 \supset \mathcal{H}_m \to \mathcal{P}_m$ is smooth. Given the target point x and the source point y, let us set $x = \Phi_m(\xi_0, \eta_0)$ and $y = \Phi_m(\xi, \eta)$, wherein (ξ_0, η_0) and $(\xi, \eta) \in \mathcal{H}_m$. Define the subset $\tilde{\mathcal{H}}_{x,m}$ in the parameter space by setting

$$\tilde{\mathcal{H}}_{x,m} = \{\, (\xi, \eta) \in \mathcal{H}_m \mid \Phi_m(\xi, \eta) \in \mathcal{P}_m \cap \mathcal{A}_x\},$$

DOI: 10.1002/nme

where $\mathcal{A}_x$ is the adjacent set introduced in Section 4.2.2. Then the elastic and acoustic singular adjacent integrals over $\mathcal{P}_m$ given in (4.6) can be rewritten as integrals over the parameter space as follows:

$$\int_{\tilde{\mathcal{H}}_{x,m}} \mathbb{G}(\Phi_m(\xi_0,\eta_0),\Phi_m(\xi,\eta))\,\boldsymbol{\phi}(\Phi_m(\xi,\eta))\,\mathrm{d}\xi\mathrm{d}\eta, \tag{4.7}$$

$$\int_{\tilde{\mathcal{H}}_{x,m}} \mathbb{T}(\Phi_m(\xi_0,\eta_0),\Phi_m(\xi,\eta))\,\boldsymbol{\psi}(\Phi_m(\xi,\eta))\,\mathrm{d}\xi\mathrm{d}\eta; \tag{4.8}$$

$$\int_{\tilde{\mathcal{H}}_{x,m}} G(\Phi_m(\xi_0,\eta_0),\Phi_m(\xi,\eta))\,\phi(\Phi_m(\xi,\eta))\,\mathrm{d}\xi\mathrm{d}\eta, \tag{4.9}$$

$$\int_{\tilde{\mathcal{H}}_{x,m}} \frac{\partial G}{\partial n}(\Phi_m(\xi_0,\eta_0),\Phi_m(\xi,\eta))\,\psi(\Phi_m(\xi,\eta))\,\mathrm{d}\xi\mathrm{d}\eta. \tag{4.10}$$

Here

$$\begin{aligned}
\boldsymbol{\phi}(\Phi_m(\xi,\eta)) &= -\hat{p}(\Phi_m(\xi,\eta))\,\mathbf{n}(\Phi_m(\xi,\eta))\,w_m(\Phi_m(\xi,\eta))\,J(\xi,\eta),\\
\boldsymbol{\psi}(\Phi_m(\xi,\eta)) &= \hat{\mathbf{u}}(\Phi_m(\xi,\eta))\,w_m(\Phi_m(\xi,\eta))\,J(\xi,\eta),\\
\phi(\Phi_m(\xi,\eta)) &= \rho\omega^2\hat{\mathbf{u}}(\Phi_m(\xi,\eta))\cdot\mathbf{n}(\Phi_m(\xi,\eta))\,w_m(\Phi_m(\xi,\eta))\,J(\xi,\eta),\\
\psi(\Phi_m(\xi,\eta)) &= \hat{p}(\Phi_m(\xi,\eta))\,w_m(\Phi_m(\xi,\eta))\,J(\xi,\eta),
\end{aligned}$$

and $J(\xi,\eta)$ is the Jacobian.

We introduce a floating partition of unity to localize the singularity. To this end, let $v(r)$ be a smooth function such that

$$v(r) = \begin{cases} 1 & \text{if } \sqrt{(\xi-\xi_0)^2+(\eta-\eta_0^2)} \leqslant r_0;\\ \\ 0 & \text{if } \sqrt{(\xi-\xi_0)^2+(\eta-\eta_0^2)} \geqslant r_1, \end{cases} \tag{4.11}$$

where r_0 and r_1 are positive constants and $r_1 > r_0$. Figure 6 shows the support of the function v. The pair v and $1-v$ forms a partition of unity in the neighborhood of x, by which the singular adjacent interactions (4.7)–(4.10) can be further decomposed into a singular part and a nonsingular one:

$$\int_{\tilde{\mathcal{H}}_{x,m}} \ldots\ v\ \mathrm{d}\xi\mathrm{d}\eta + \int_{\tilde{\mathcal{H}}_{x,m}} \ldots\ (1-v)\ \mathrm{d}\xi\mathrm{d}\eta.$$

Again, the nonsingular part may be evaluated accurately by the trapezoidal rule. The evaluation of singular part is described as follows.

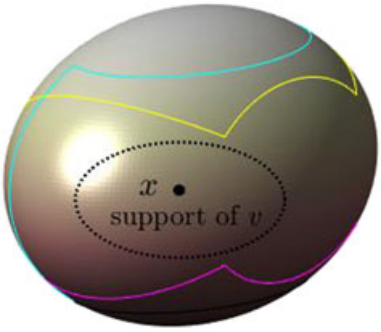

Figure 6. Floating partition of unity associated with the target point x.

DOI: 10.1002/nme

Define the local polar coordinate

$$\xi = \xi_0 + \rho\cos\theta, \tag{4.12}$$

$$\eta = \eta_0 + \rho\sin\theta. \tag{4.13}$$

Note that the integral kernels $\mathbb{G}(x,y)$, $G(x,y)$, and $\partial G/\partial n(x,y)$ are weakly singular, and there holds:

$$\mathbb{G}(x,y) \sim O\left(\frac{1}{|x-y|}\right), \quad G \sim O\left(\frac{1}{|x-y|}\right), \quad \text{and} \quad \partial G/\partial n(x,y) \sim O\left(\frac{(x-y)\cdot\mathbf{n}}{|x-y|^3}\right).$$

Therefore, in the polar coordinate, the associated singular integrals of (4.7) and (4.9) take the forms of

$$\int_0^{2\pi}\int_0^{r_1} O\left(\frac{1}{|x-y|}\right)\rho\, v(\rho)\,\mathrm{d}\rho\mathrm{d}\theta,$$

and the singular integral of (4.10) takes the form of

$$\int_0^{2\pi}\int_0^{r_1} O\left(\frac{(x-y)\cdot\mathbf{n}}{|x-y|^3}\right)\rho\, v(\rho)\,\mathrm{d}\rho\mathrm{d}\theta.$$

Using the fact that the limits

$$\lim_{|x-y|\to 0}\frac{\rho}{|x-y|} = c_1, \lim_{|x-y|\to 0}\frac{(x-y)\cdot\mathbf{n}}{|x-y|^2} = c_2$$

for some constants c_1 and c_2 if Γ is a smooth surface, we deduce that the associated integrands in the polar coordinate are smooth functions of ρ and, as such, can be evaluated accurately by Gaussian quadratures. For instance, assume that the fluid–structure interface Γ is a sphere and the associated covering cube is decomposed into 10^3 small cubic cells. Let $v(r)$ be a smooth function as defined in (4.11) with $r_0 = 0.005$ and $r_1 = 0.04$ such that the image of its support is contained in the adjacent set $\mathcal{A}_x$. Then as shown in Table I, 6 Gauss points in each direction are sufficient to obtain four digits of accuracy for approximating the integral $\int_0^{2\pi}\int_0^{r_1} v(\rho)\,\mathrm{d}\rho\mathrm{d}\theta$.

The singular part of (4.8) is treated by a semi-classical method. More precisely, let

$$\mathbf{W}(\xi,\eta) = \mathbb{T}(\Phi_m(\xi_0,\eta_0),\Phi_m(\xi,\eta))\,\boldsymbol{\psi}(\Phi_m(\xi,\eta))\,v$$

and

$$\tilde{\mathbf{W}}(\rho,\theta) = \mathbf{W}(\xi_0+\rho\cos\theta,\eta_0+\rho\sin\theta)\,\rho.$$

Then the singular integral in the polar coordinate takes the form of $\int_0^{r_1}\int_0^{2\pi}\tilde{\mathbf{W}}(\rho,\theta)\,\mathrm{d}\theta\mathrm{d}\rho$, where we have used the fact that v vanishes for $\rho > r_1$. Because of the strong singularity of the Green tensor $\mathbb{T}$, the integrand $\tilde{\mathbf{W}}(\rho,\theta)$ adopts a Laurent series expansion with respect to ρ:

$$\tilde{\mathbf{W}}(\rho,\theta) = \frac{\tilde{\mathbf{W}}_{-1}(\theta)}{\rho} + O(1), \tag{4.14}$$

Table I. Accuracy of the Gaussian quadrature.

n_g	4	6	10	20
I_{n_g}	0.1509867095	0.1496400769	0.1497077795	0.1496979270
e_{n_g}	1.29×10^{-3}	5.78×10^{-5}	9.94×10^{-6}	8.63×10^{-8}

I_{n_g} is a numerical integral value obtained with n_g Gauss points in each direction, and e_{n_g} is the associated numerical error.

DOI: 10.1002/nme

wherein the explicit expression $\tilde{\mathbf{W}}_{-1}(\theta)$ is derived in the Appendix A. In this way, we obtain the following formula to evaluate the singular integral:

$$\int_0^{r_1}\int_0^{2\pi} \tilde{\mathbf{W}}(\rho,\theta)\,\mathrm{d}\theta\mathrm{d}\rho = \mathcal{I}_0 + \mathcal{I}_{-1},$$

where the regular part

$$\mathcal{I}_0 = \int_0^{r_1}\int_0^{2\pi} \tilde{\mathbf{W}}(\rho,\theta) - \frac{\tilde{\mathbf{W}}_{-1}(\theta)}{\rho}\,\mathrm{d}\theta\mathrm{d}\rho$$

and the singular part

$$\mathcal{I}_{-1} = \int_0^{r_1}\int_0^{2\pi} \frac{\tilde{\mathbf{W}}_{-1}(\theta)}{\rho}\,\mathrm{d}\theta\mathrm{d}\rho.$$

Here, the singular integral $\mathcal{I}_{-1}$ is understood in the sense of Cauchy principle. By noting that $\tilde{\mathbf{W}}_{-1}(\theta) = -\tilde{\mathbf{W}}_{-1}(\theta+\pi)$ (cf. Appendix A), we have $\mathcal{I}_{-1} = 0$. On the other hand, the regular part $\mathcal{I}_0$ is smooth and can be evaluated accurately by Gaussian quadratures.

Remark 1
The values of density functions $\boldsymbol{\phi}$, $\boldsymbol{\psi}$, ϕ, and ψ are known only on the Cartesian grid points in each patch, and their values on radial quadrature points of $\mathcal{I}_0$ are not defined. To obtain the function values at those radial integration point, the following standard fast interpolation process is applied [45, 46]*:*

1. *Based on the function values on the Cartesian grid points, obtain the Fourier coefficients of $\boldsymbol{\phi}$, $\boldsymbol{\psi}$, ϕ, and ψ along the grid lines via FFT.*
2. *Evaluate the function values and its derivatives on a refined grid via FFT.*
3. *Construct a cubic interpolating polynomial on each interval of the refined grid using the values obtained in 2.*

This process yields accurate interpolations by cubic splines, and it only contributes a negligible amount of computation cost with the application of FFT.

4.4. Fast nonsingular integration

The fast evaluation of non-adjacent nonsingular interactions in (4.6) is based on the equivalent source representations. In more details, for cubic cells c_{jkl} $(j,k,l = 1,2,\ldots,L)$ introduced in Section 4.2.2, we define Cartesian grid points on each face of cubic cell and for all L^3 cells with an identical grid size h. Let Π^s $(s = 1,2,3)$ be the set of all Cartesian grid points with the corresponding cell faces parallel to the plane $x_s = 0$ $(s = 1,2,3)$; then Π^s lies on $L+1$ parallel planes, where the grids on each plane are shown in Figure 7. For each cubic cell c_{jkl}, we introduce two squares, $\mathcal{Q}^{s,1}_{jkl}$ and $\mathcal{Q}^{s,2}_{jkl}$ (the dashed squares in Figure 7), that contain its two cell faces parallel to the plane $x_s = 0$. The equivalent sources associated with the cell are prescribed over a subset of Cartesian grid points as given by

$$\Pi^s_{jkl} = \Pi^s \cap \left(\mathcal{Q}^{s,1}_{jkl} \cup \mathcal{Q}^{s,2}_{jkl}\right), \quad s = 1,2,3. \tag{4.15}$$

Now, let

$$\hat{\mathbf{t}} = -\hat{p}\,\mathbf{n}, \quad \text{and} \quad \widehat{p_n} = \rho_f \omega^2 \hat{\mathbf{u}}\cdot\mathbf{n}.$$

The discretized version of the nonsingular integrals

$$\sum_{m=1}^{M}\int_{\mathcal{P}_m\cap\mathcal{A}_x^c}\left[\mathbb{G}(x,y)\hat{\mathbf{t}}(y)w_m(y) - \mathbb{T}(x,y)\hat{\mathbf{u}}(y)w_m(y)\right]\mathrm{d}s_y \tag{4.16}$$

DOI: 10.1002/nme

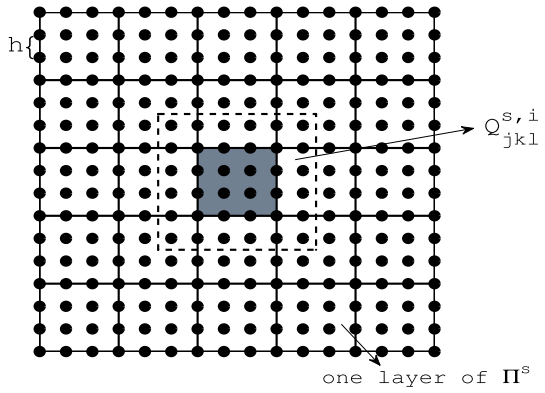

Figure 7. One layer of the Cartesian grid points Π^s. For a cubic cell c_{jkl}, the equivalent source points on the face (gray square) is given by $\Pi^s \cap \left(\mathcal{Q}^{s,1}_{jkl} \cup \mathcal{Q}^{s,2}_{jkl}\right)$, where $\mathcal{Q}^{s,i}_{jkl}$ $(i = 1, 2)$ is the dashed square containing the gray cell face $(i = 1, 2)$.

and

$$\sum_{m=1}^{M} \int_{\mathcal{P}_m \cap \mathcal{A}_x^c} \left[G(x, y)\widehat{p_n}(y) w_m(y) - \frac{\partial G}{\partial n}(k; x, y)\ \hat{p}(y) w_m(y) \right] \mathrm{d}s_y \tag{4.17}$$

can be viewed as potentials because of elastic/acoustic monopoles and dipoles located on the surface points, which are called 'true sources'. For each cubic cell introduced in Section 4.2.2, we approximate the field radiated from the true sources inside c_{jkl} by the field radiated from the associated equivalent sources located at Cartesian grid points Π^s_{jkl} defined in (4.15). In practice, the width of $\mathcal{Q}^{s,1}_{jkl}$ and $\mathcal{Q}^{s,2}_{jkl}$ is equal or larger than the length of the diagonal of the cell faces to guarantee an accurate approximation.

Let $\boldsymbol{\zeta}^s_{jkl}$ and $\boldsymbol{\sigma}^s_{jkl}$ be the elastic monopoles and dipoles, respectively, on each grid point $x^s_{jkl,n} \in \Pi^s_{jkl}$ $(n = 1, 2, \ldots, N_{equiv})$ and ζ^s_{jkl} and σ^s_{jkl} be the acoustic monopoles and dipoles, respectively. Then the fields induced by these elastic and acoustic equivalent sources are

$$\boldsymbol{\varphi}^{equiv,s}_{jkl}(x) = \sum_{n=1}^{N_{equiv}} \mathbb{G}\left(x, x^s_{jkl,n}\right) \boldsymbol{\zeta}^s_{jkl,n} + \mathbb{T}\left(x, x^s_{jkl,n}\right) \boldsymbol{\sigma}^s_{jkl,n}, \tag{4.18}$$

$$\varphi^{equiv,s}_{jkl}(x) = \sum_{n=1}^{N_{equiv}} G\left(x, x^s_{jkl,n}\right) \zeta^s_{jkl,n} + \frac{\partial G}{\partial n}\left(x, x^s_{jkl,n}\right) \sigma^s_{jkl,n}. \tag{4.19}$$

It can be shown that as long as x is not adjacent to c_{jkl}, $\boldsymbol{\varphi}^{equiv,s}_{jkl}(x)$ and $\varphi^{equiv,s}_{jkl}(x)$ are accurate approximations of the fields $\boldsymbol{\varphi}^{true}_{jkl}(x)$ and $\varphi^{true}_{jkl}(x)$ induced by the true sources within the cell. The equivalent sources $\boldsymbol{\zeta}^s_{jkl,n}$, $\boldsymbol{\sigma}^s_{jkl,n}$, $\zeta^s_{jkl,n}$, and $\sigma^s_{jkl,n}$ can be obtained by solving the following overdetermined linear systems:

$$\mathbb{B}_e \begin{bmatrix} \boldsymbol{\zeta} \\ \boldsymbol{\sigma} \end{bmatrix} = \mathbf{b}_e, \quad \mathbb{B}_p \begin{bmatrix} \zeta \\ \sigma \end{bmatrix} = \mathbf{b}_p. \tag{4.20}$$

Here, the matrices $\mathbb{B}_e$ and $\mathbb{B}_p$ correspond to the evaluation of (4.18) and (4.19) at n^{coll} collocation points located on the boundary of the adjacent set $\mathcal{A}_x$. The vectors $\mathbf{b}_e$ and $\mathbf{b}_p$ are the elastic and acoustic fields at collocation points generated by true sources. Because all the cells are identical, the QR decomposition of $\mathbb{B}_e$ and $\mathbb{B}_p$ needs only be computed once and stored for repeated use.

We first evaluate the non-adjacent interactions (4.16) and (4.17) for the Cartesian grid points on Π^s. Using the equivalent source approximation, this reduces to the calculations of convolutions (4.18) and (4.19) on Π^s subtracted by the contributions from adjacent cubic cells. That is, for the target point $x \in \Pi^s$,

DOI: 10.1002/nme

$$\boldsymbol{\varphi}^{equiv,s}(x) = \boldsymbol{\varphi}^{equiv,s}_{total}(x) - \boldsymbol{\varphi}^{equiv,s}_{adj}(x) \quad \text{and} \quad \varphi^{equiv,s}(x) = \varphi^{equiv,s}_{total}(x) - \varphi^{equiv,s}_{adj}(x),$$

where the convolution on the whole Cartesian grids Π^s and the adjacent contributions are given, respectively, by

$$\boldsymbol{\varphi}^{equiv,s}_{total}(x) = \sum_{y\in\Pi^s} \mathbb{G}(x,y)\boldsymbol{\zeta}^s_y + \mathbb{T}(x,y)\boldsymbol{\sigma}^s_y, \quad \varphi^{equiv,s}_{total}(x) = \sum_{y\in\Pi^s} G(x,y)\zeta^s_y + \frac{\partial G}{\partial n}(x,y)\sigma^s_y, \tag{4.21}$$

and

$$\boldsymbol{\varphi}^{equiv,s}_{adj}(x) = \sum_{c_{jkl}\ adjacent\ to\ x} \boldsymbol{\varphi}^{equiv,s}_{jkl}(x), \quad \varphi^{equiv,s}_{adj}(x) = \sum_{c_{jkl}\ adjacent\ to\ x} \varphi^{equiv,s}_{jkl}(x). \tag{4.22}$$

The convolutions just shown, which are defined over Cartesian grid points, can be evaluated in a fast manner with the FFT. By carrying out the procedure for $s = 1, 2, 3$, we obtain $\boldsymbol{\varphi}^{equiv,s}$ and $\varphi^{equiv,s}$ for the Cartesian grid points on all faces of the cubic cells.

Finally, the field values at true source locations inside each cell are obtained by solving the associated Dirichlet problems for the elastic and acoustic wave equations. For a non-resonant cell, the problems are uniquely solvable. We adopt plane wave expansions for the solutions (cf. [50, 51]) such that

$$\begin{aligned}\hat{\mathbf{u}} &= \hat{\mathbf{u}}_P + \hat{\mathbf{u}}_{SH} + \hat{\mathbf{u}}_{SV} \\ &= \sum_{j=1}^{N_d} \left(\alpha_{p,j}\ \hat{d}_j\ e^{i\kappa_p \hat{d}_j\cdot x} + \alpha_{sh,j}\ \hat{d}_j^{\perp}\ e^{i\kappa_s \hat{d}_j\cdot x} + \alpha_{sv,j}\ (\hat{d}_j \times \hat{d}_j^{\perp})\ e^{i\kappa_s \hat{d}_j\cdot x}\right).\end{aligned} \tag{4.23}$$

$$\hat{p} \quad = \sum_{j=1}^{N_d} \beta_j e^{ik\hat{d}_j\cdot x}. \tag{4.24}$$

Here, $\hat{d}_j$ is the unit wave vector, and $\hat{d}_j^{\perp}$ denotes the vector perpendicular to $\hat{d}_j$. $\alpha_{p,j}$, $\alpha_{sh,j}$, and $\alpha_{sv,j}$ are the expansion coefficients for elastic P-wave, SH-wave, and SV-wave, respectively, and β_j are the expansion coefficients for the pressure field. The coefficients are chosen such that the resulting wave fields match the wave fields on the Cartesian grid points of the cell faces, which are obtained in the previous step via the FFT. This also involves solving an overdetermined linear system. Again, note that each cell is identical; hence, the QR decomposition of coefficients matrices needs only be computed once and stored for repeated use.

4.5. Computational cost

To achieve sufficient accuracy, the total number M_Γ of equivalent sources on each parallel plane of Π_s is approximately equal to the number of points required by the Nyquist sampling theorem. That is, $M_\Gamma \sim O(N_\Gamma)$. The main computational cost for non-adjacent interactions consists of three parts: convolutions (4.21) and (4.22), identification of equivalent sources in (4.20) and solution for the coefficients in the plane wave expansions (4.23) and (4.24). The convolutions on the Cartesian grid points Π^s via the FFT yields a computational cost of $O(N_\Gamma L \log(N_\Gamma L))$. As discussed in Section 4.2.2, each of non-empty cells contains approximately $O\left(N_\Gamma/L^2\right)$ surface points. Hence, the equivalent source identification and plane wave expansions would require $O\left(N_\Gamma^2/L^4\right)$ operations for each non-empty cell, because the QR decomposition can be computed ahead and stored for repeated use. Consequently, the associated computational cost for $O(L^2)$ non-empty cells is $O\left(N_\Gamma^2/L^2\right)$.

In light of the fact that the adjacent interactions in (4.6) require $O\left(N_\Gamma^2/L^2\right)$ operations for all target points, the whole algorithm for one matrix-vector product associated with the discretization of the integrals in (4.1) gives rise to a total cost of $O\left(N_\Gamma^2/L^2\right) + O(N_\Gamma L \log(N_\Gamma L))$. By choosing $L = O\left(N_\Gamma^{1/3}\right)$, an optimal cost of $O\left(N_\Gamma^{4/3}\log N_\Gamma\right)$ operations is achieved.

DOI: 10.1002/nme

The algorithm gives rise to a marginally increased memory requirement compared with that of the non-accelerated one. The equivalent sources on the Cartesian grid points and the evaluation of the FFT require additional storage of $O(N_\Gamma L)$. On the other hand, the storage of the QR decomposition matrices associated with the equivalent source identifications and the plane wave decompositions is negligible.

5. NUMERICAL EXAMPLES

Several numerical examples are presented in this section to illustrate the efficiency and accuracy of the proposed numerical method. Both the radiation and scattering problems are studied. The first example investigates the boundary integral equation (BIE) solver in the frequency-domain, which is essential to the speedup of the sampling procedure in the main algorithm and the accuracy of the time-domain solution. The second example studies the accuracy of the proposed frequency-domain approach for transient analysis when the elastic structure is a unit ball, and the last example considers the acoustic–structure interaction with more complex geometries.

Example 1. (*Accuracy and efficiency of the frequency-domain BIE solver*). Consider a unit ball embedded in an infinite acoustic fluid medium. The Lamé constants and the density for the elastic medium are $\lambda = 24$, $\mu = 12$, and $\rho_e = 3$, respectively. The fluid velocity and density are $c_f = 1.5$ and $\rho_f = 1$, respectively. We consider both the radiation problem (Figure 8, left) and the scattering problem (Figure 8, right).

For the radiation problem, assume that the force in (3.2) is given by $\hat{\mathbf{f}} = \nabla\delta(x)$, where $\delta(x)$ is the Dirac delta function. The analytical solution admits an expansion by spherical harmonics and Bessel functions, which is derived in Appendix B.1. To obtain the numerical solution, the sphere interface is covered by four overlapping patches. The solutions are calculated for two sets of discretizations, with 64×64 and 128×128 points over each patch, respectively. The discretization and acceleration parameters are given in Table II. The number of patches and the discretization points on each patch are given in the first column. L is the number of cubic cells in each direction, N_{equiv} is the number of equivalent sources on two faces of each cell as defined by (4.15) and n_{coll} is the number of collocation points used to obtain the equivalent sources in (4.20). The tolerance for the GMRES iteration is set as 10^{-5} when solving the associated linear system. We define the relative L^2-norm errors for the displacement vector of the elastic solid and the pressure field of the fluid by

$$\varepsilon_{u,2} = \frac{\left(\int_\Gamma |\hat{\mathbf{u}}^{num} - \hat{\mathbf{u}}^a|^2 \mathrm{d}x\right)^{1/2}}{\left(\int_\Gamma |\hat{\mathbf{u}}^a|^2 \mathrm{d}x\right)^{1/2}} \quad \text{and} \quad \varepsilon_{p,2} = \frac{\left(\int_\Gamma |\hat{p}^{num} - \hat{p}^a|^2 \mathrm{d}x\right)^{1/2}}{\left(\int_\Gamma |\hat{p}^a|^2 \mathrm{d}x\right)^{1/2}},$$

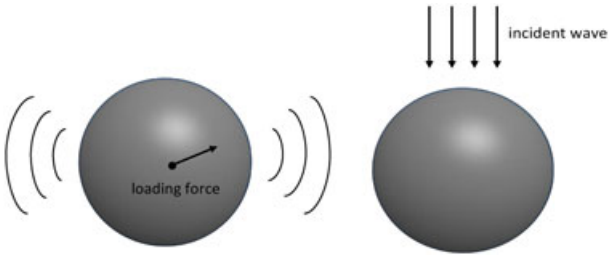

Figure 8. Left: radiation problem where the force is excited inside the elastic structure; Right: scattering problem where an incident wave impinges on a homogeneous elastic structure.

Table II. Accuracy of the boundary integral equation method.

Discretization	L	N_{equiv}	n_{coll}	$\varepsilon_{u,2}$	$\varepsilon_{p,2}$
$4 \times 64 \times 64$	12	162	602	8.89×10^{-3}	4.46×10^{-3}
$4 \times 128 \times 128$	18	162	602	4.47×10^{-4}	5.76×10^{-4}

DOI: 10.1002/nme

where $\hat{\mathbf{u}}^a$ and $\hat{p}^a$ represent the analytical solution. The corresponding numerical errors are shown in the last two columns of Table II, which demonstrate the convergence and high-order accuracy of the proposed algorithm. We also plot the computed pressure field obtained by the second discretization and the associated error in the acoustic medium on the plane $x_2 = 0$ in Figure 9. The computational cost for the evaluation of the matrix-vector product for each iteration of GMRES process is recorded in Table III. To make a comparison, the computational cost using the traditional non-accelerated trapezoidal rule is also shown. It is seen that the proposed frequency-domain boundary integral equation method is much more efficient than the non-accelerated one.

For the scattering problem, assume that a plane wave $\hat{p}^{inc} = e^{-i\kappa_f x_3}$ impinges upon the elastic structure from the negative x_3 direction (Figure 8, right). After the scattering, the total pressure field $\hat{p} = \hat{p}^{inc} + \hat{p}^s$, where $\hat{p}^s$ is the scattered field. Again, the analytical solution may be expressed by spherical harmonics and Bessel functions as given in Appendix B.2. To obtain the numerical solution, the same acceleration parameters as in the radiation problem are used. The computational cost for the accelerated and non-accelerated algorithms is given in Table IV. To demonstrate the accuracy of the boundary integral equation approach, the computed scattered field and the associated error on the plane $x_2 = 0$ are demonstrated in Figure 10 for a discretization with four patches and 128×128 points on each patch. It is seen that the proposed algorithm exhibits high-order accuracy.

Example 2. (*Accuracy of the numerical method for transient acoustic–structure interactions*). We apply the combination of the exponential window technique and the fast frequency-domain algorithm to solve the time-domain coupled problem (2.1)–(2.5). The elastic solid is a unit ball and is surrounded by the acoustic medium. The Lamé constants and the density for the elastic medium are

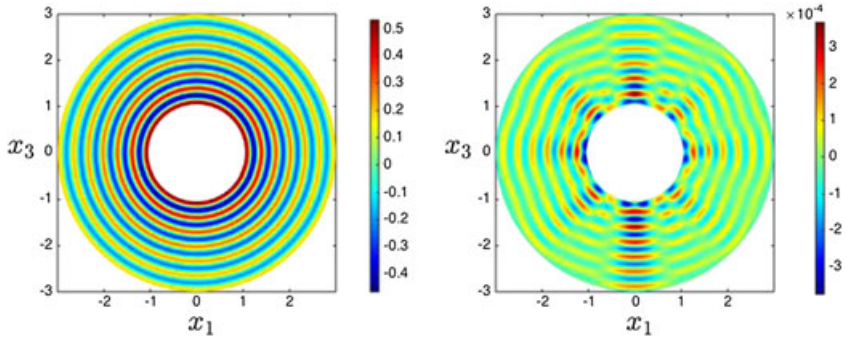

Figure 9. Real part of the pressure field (left) and the associated numerical error (right) in the acoustic medium on the plane $x_2 = 0$ for the radiation problem.

Table III. Computational cost of the accelerated and non-accelerated algorithms for the radiation problem when the generalized minimal residual iteration is applied.

Discretization	L	N_{equiv}	n_{coll}	Time/iter. (accl.) (min)	T_s (min)	T_{ns} (min)	Time/iter. (no accel.)(min)	Iteration number
$4 \times 64 \times 64$	12	162	602	1.55	0.67	0.88	4.66	113
$4 \times 128 \times 128$	18	162	602	5.3	2.68	2.62	59.38	41

T_s and T_{ns} denote the computational time for the singular and nonsingular integral evaluations, respectively, at each iteration.

Table IV. Computational cost of the accelerated and non-accelerated algorithms for the scattering problem.

Discretization	L	N_{equiv}	n_{coll}	Time/iter. (accl.) (accl.) (min)	T_s (min)	T_{ns} (min)	Time/iter. (no accel.) (min)	Iteration number
$4 \times 64 \times 64$	12	162	602	1.55	0.67	0.88	4.66	79
$4 \times 128 \times 128$	18	162	602	5.3	2.68	2.62	59.38	87

DOI: 10.1002/nme

$\lambda = 6$, $\mu = 12$, and $\rho_e = 1.2$, respectively, and the fluid velocity and density are $c_f = 0.25$ and $\rho_f = 1$, respectively.

Let us consider the radiation problem with a loading force specified by

$$\mathbf{f}(x,t) = F_0 f_1(t)\mathbf{f}_2(x).$$

Here, the magnitude $F_0 = \lambda + 2\mu$, $\mathbf{f}_2(x) = \nabla\delta(x)$, and $f_1(t)$ represents a scaled Ricker pulse as shown in Figure 11. More explicitly,

$$f_1(t) = (1 - a^2(t-b)^2/2)e^{-a^2(t-b)^2/4},$$

wherein $a = 6$ and $b = 1.5$. The Fourier transform of the Ricker pulse, $\hat{f}_1(\omega)$, is also plotted in Figure 11. The analytical solution for the time-domain problem (2.1)–(2.5) is evaluated by the inverse transform

$$\mathbf{u}^a(x,t) = \int_{-\infty}^{+\infty} \widehat{\mathbf{u}^a}(x,\omega)e^{-i\omega t}\,\mathrm{d}\omega \quad \text{and} \quad p^a(x,t) = \int_{-\infty}^{+\infty} \widehat{p^a}(x,\omega)e^{-i\omega t}\,\mathrm{d}\omega,$$

where the solution at each fixed frequency is given in Appendix B.1.

To obtain the numerical solution for $t \in [0,3]$ with the exponential window technique, following the discussions in Section 3, we expand the time window with an enlarged time period $T = 6$ and choose the damping parameter $\eta = \log 10/3$. As such the signal is damped with a factor of 10^{-2} at the end of the period, and one-digit precision is lost when performing the recovery procedure (3.6) for $t \in [0,3]$. The number of sampling points is set as $N_\omega = 400$; thus, the time resolution $\Delta t = T/N_\omega$, and the frequency resolution $\Delta\omega = 2\pi/T$. The frequency-domain wave fields $\hat{\mathbf{u}}$ and $\hat{p}$ are obtained at the complex frequencies $\omega_n = n\Delta\omega + i\eta$ $(n = 0, 1, \ldots, N_\omega/2)$ by solving (3.2)–(3.5) with the fast integral equation approach described in Section 4. The fluid–structure interface is discretized with sufficient number of surface points such that three-digit accuracy is achieved for

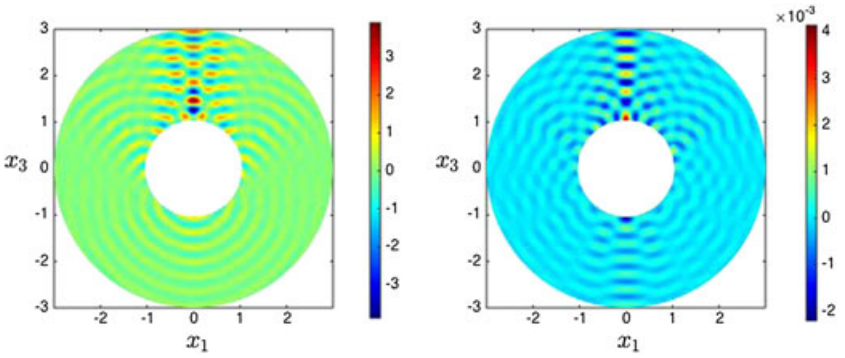

Figure 10. Real part of the scattered pressure field (left) and the associated numerical error (right) in the acoustic medium on the plane $x_2 = 0$ for the scattering problem.

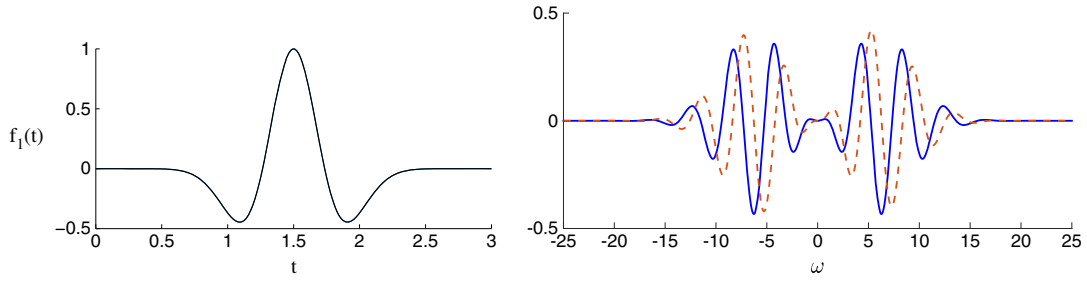

Figure 11. Left: scaled Ricker pulse $f_1(t)$. Right: Fourier transform of the pulse. The solid and dash lines denote the real and imaginary parts, respectively.

DOI: 10.1002/nme

the frequency-domain solutions. It is also observed from Figure 11 that the significant frequency band of the Ricker pulse is $[-20, 20]$; hence, it is sufficient to sample the solutions for the first 21 frequencies only, which are implemented in parallel. The solutions for the last $N_\omega/2-1$ frequencies are obtained then by evaluating the following complex conjugate:

$$\hat{\mathbf{u}}(x, \omega_n) = \overline{\hat{\mathbf{u}}(x, \omega_{N_\omega - n})}, \quad \hat{p}(x, \omega_n) = \overline{\hat{p}(x, \omega_{N_\omega - n})}, \qquad n = N_\omega/2+1, N_\omega/2+2, \ldots, N_\omega-1.$$

Finally, the transient signals are computed via the inverse DFT and scaled with a factor of $e^{\eta t}$ as described in Section 3.

The computed pressure field and the associated numerical errors at $(0, 0, 1.05)$ and $(0, 0, 1.2)$ are shown in Figure 12. We also plot the pressure field on the plane $x_2 = 0$ in the acoustic medium for $t = 3$ in Figure 13. It is observed that the proposed frequency-domain approach yields two-digit accuracy for the obtained solution. On the other hand, a direct discrete Fourier transform method without the exponential window technique gives rise to a pressure field with large numerical errors as demonstrated in Figure 14. This is because the free vibration is not damped out at the end of the period and the wrap-around errors incurred in the DFT pollute the numerical solution.

Example 3. (*Transient analysis for acoustic–structure interaction problems with complex geometry*). In this example, we consider the case when the elastic structure has a bone shape as shown

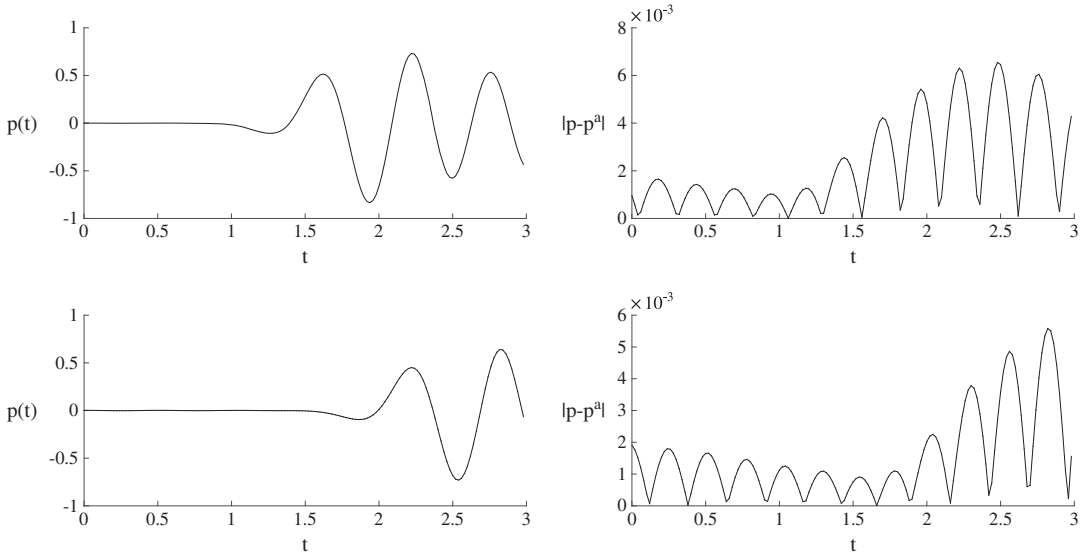

Figure 12. Left column: computed pressure field at the locations $(0, 0, 1.05)$ and $(0, 0, 1.2)$ for $t \in [0, 3]$. Right column: the associated numerical error at specified locations.

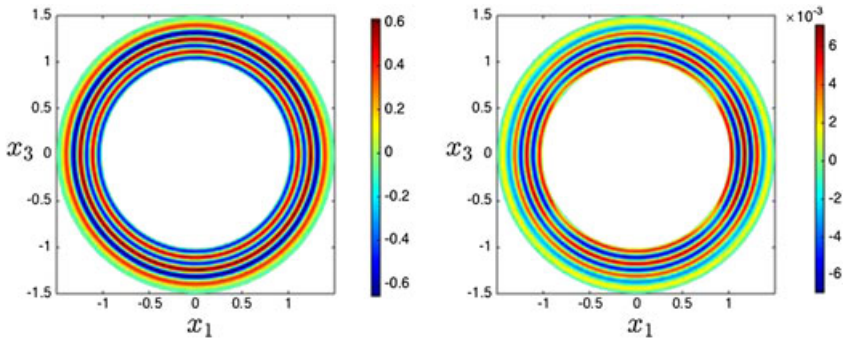

Figure 13. Pressure field (left) and the associated numerical error (right) in the acoustic medium on the plane $x_2 = 0$.

DOI: 10.1002/nme

in Figure 15 and is immersed in water. The associated radiation problem arises in the ultrasound acousto-vibrography, where two focused ultrasound beams are used to vibrate the bone [1]. The elastic solid has a length of 4 cm. Its width is 7 and 13 mm in the center and at the two ends, respectively. The density of the solid is set as $\rho_e = 1840\,\mathrm{kg/m^3}$. The Young modulus has a value of 9.8×10^9 Pa, and the Poisson ratio for the elastic solid is 0.374. With these physical parameters, the P-wave and S-wave speed is 3103 and 1392 m/s, respectively, in the solid. The water has a density of $1000\,\mathrm{kg/m^3}$ and a wave speed of 1484 m/s. Both the radiation and scattering problems are investigated in the following.

For the radiation problem, a localized radiation force pointing in the x direction is excited in the center of the elastic solid at $t = 0$ (Figure 15, middle). That is, the force takes the form of

$$\mathbf{f}(x,t) = f(t)\delta(x)[1,0,0]^T,$$

where $f(t)$ is the short Ricker pulse with a duration of about 20 μs as shown in Figure 16. The first and second troughs of the pulse occurs at $t = 8$ and 16 μs, respectively, and the crest of the

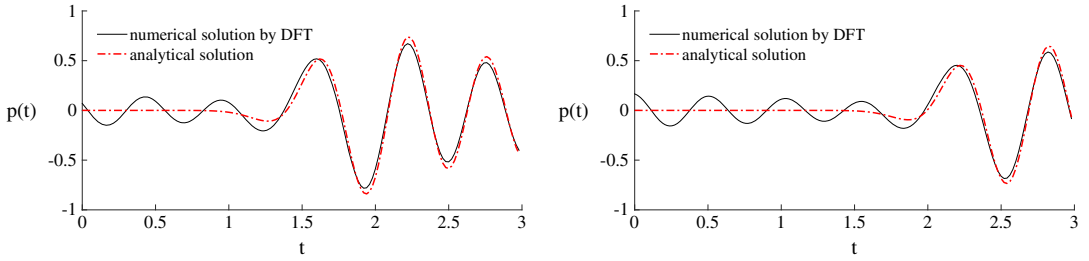

Figure 14. Pressure field obtained at $(0, 0, 1.05)$ and $(0, 0, 1.2)$ for $t \in [0, 3]$ via the discrete Fourier transform without the exponential window technique.

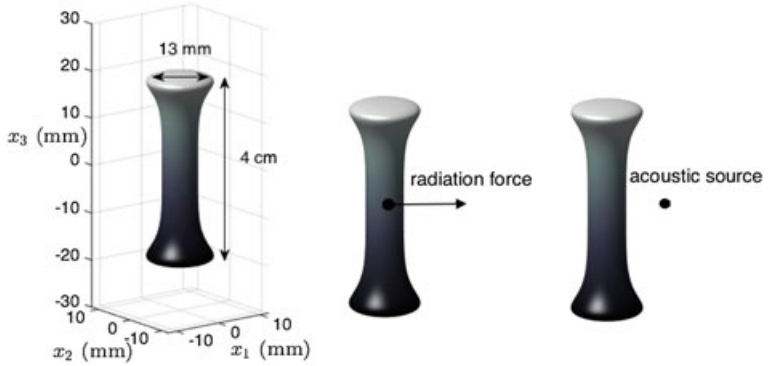

Figure 15. Geometry of the bone shape elastic structure (left) and the setup for the radiation problem (middle) and the scattering problem (right), respectively.

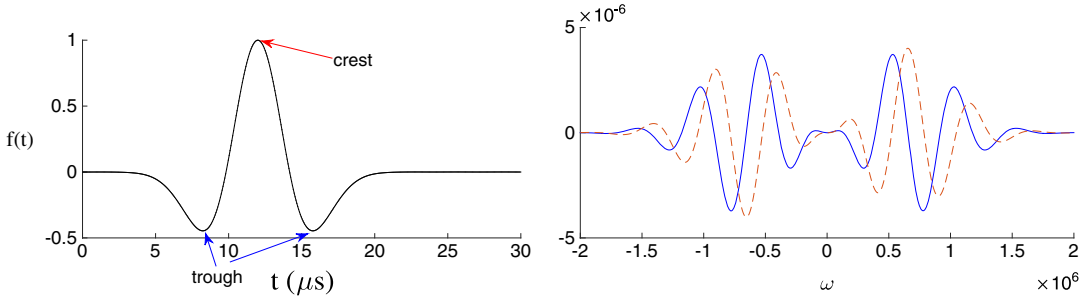

Figure 16. Left: scaled Ricker pulse $f(t)$ with a short duration. Right: Fourier transform of the pulse. The solid and dash lines denote the real and imaginary parts, respectively.

DOI: 10.1002/nme

pulse occurs at $t = 12\,\mu$s. We seek to obtain the sound pressure in water for $0 < t \leqslant 100\,\mu$s and set the time period $T = 200\,\mu$s in the DFT. The damping parameter is chosen as $\eta = 10^4 \log 10$ such that the signal is damped with a factor of 10^{-2} at the end of the period, and the number of sampling points is $N_\omega = 400$. Note that the significant frequency band of the Ricker pulse is $[-2 \times 10^6, 2 \times 10^6]$ (cf. Figure 16), and it is sufficient to solve for the frequency-domain problem (3.2)–(3.5) at $\omega_n = n\Delta\omega + i\eta$ for the first 80 frequencies only. In the acceleration strategy for the boundary integral equation solver, a three-dimensional slab instead of a cube is used to contain the elongated structure considered here. Correspondingly, the number of cubic cells in each direction is chosen adaptively to obtain an optimal computational cost. For example, there are 8, 8, and 20 cells in the x_1, x_2, and x_3 directions, respectively, for the acceleration algorithm at $\omega = \omega_{80}$.

With the proposed frequency-domain approach, the pressure field on the plane $x_2 = 0$ is shown in Figure 17 for $t = 9$, 13, 17, and 28 μs. Note that the arrival time from the location of the radiation force to the boundary of the elastic solid at $x_3 = 0$ is approximately 1 μs. Therefore, the first three plots are the pressure field when the first trough, the crest, and the second trough of the short pulse reach the boundary of the elastic structure at $x_3 = 0$, respectively. It is seen that the numerical solution accurately captures the radiation behavior of the pressure field in the acoustic medium. The fourth plot is the pressure field at $t = 28\,\mu$s, which clearly demonstrates the multiple reflections of the wave fields in the acoustic–structure system. In addition, we also plot the pressure field at the locations of $(-5\,\text{mm}, 0, 0)$ and$(5\,\text{mm}, 0, 0)$ for $0 < t \leqslant 100\,\mu s$ in Figure 18.

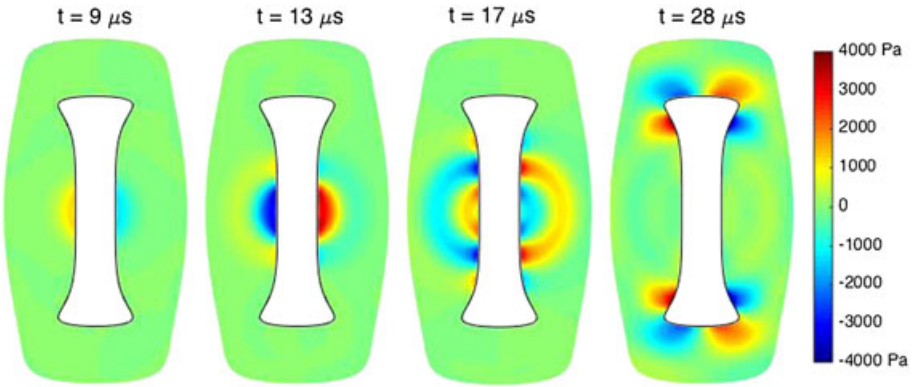

Figure 17. The pressure field on the plane $x_2 = 0$ for $t = 9\,\mu$s, 13 μs, 17 μs, and 28 μs (radiation problem).

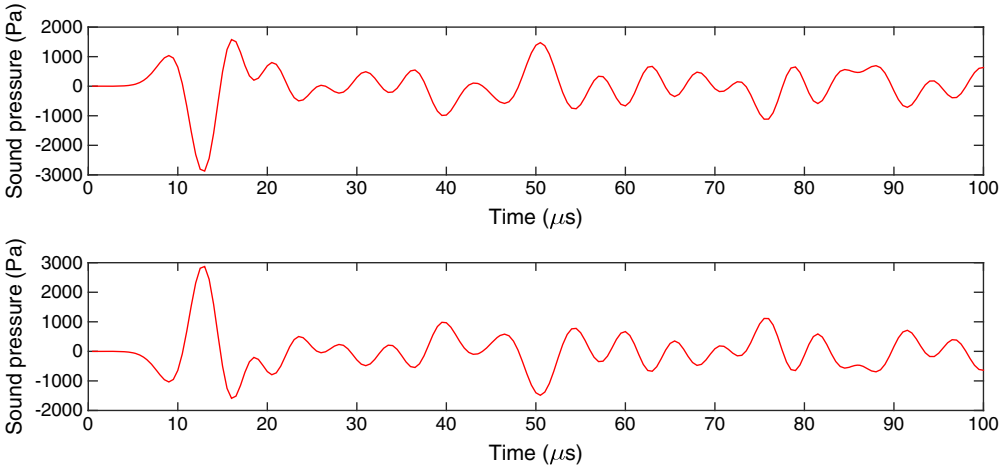

Figure 18. The pressure field at the locations of $(-5\text{mm}, 0, 0)$ (top) and $(5\text{mm}, 0, 0)$ (bottom) in the time period $0 < t \leqslant 100\mu s$ (radiation problem).

DOI: 10.1002/nme

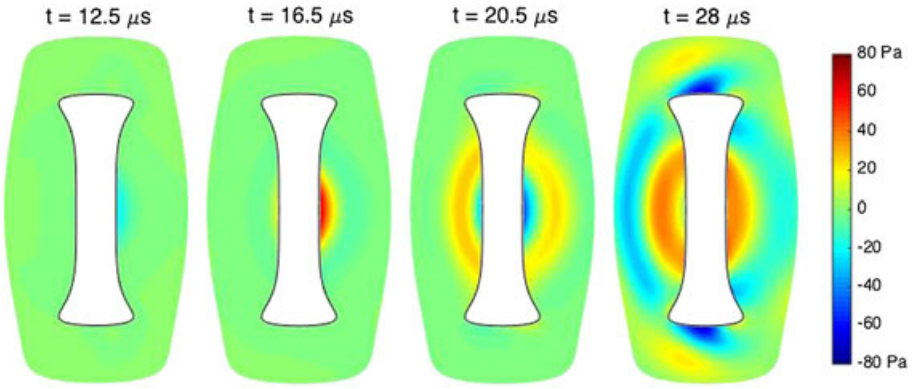

Figure 19. The scattered pressure field on the plane $x_2 = 0$ for $t = 12.5\ \mu$s, $16.5\ \mu$s, $20.5\ \mu$s, and $28\ \mu$s (scattering problem).

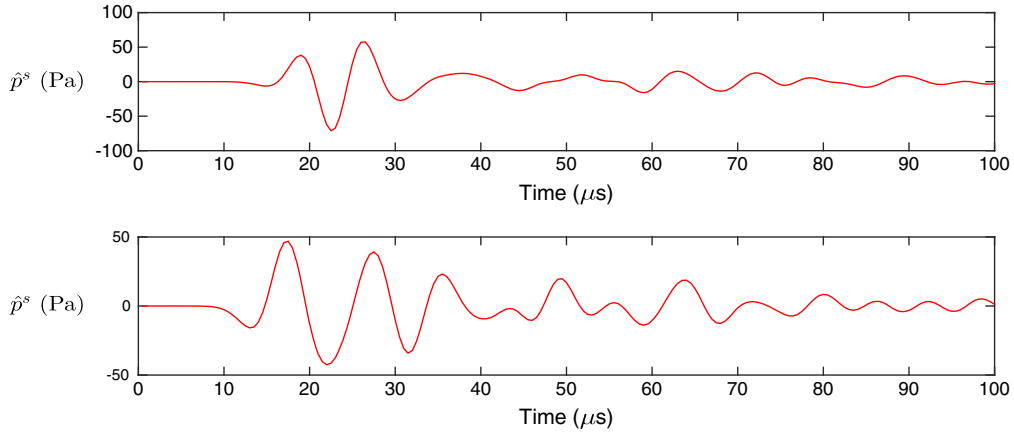

Figure 20. The scattered pressure field at the locations of $(-5\text{mm}, 0, 0)$ (top) and $(5\text{mm}, 0, 0)$ (bottom) in the time period $0 < t \leqslant 100\mu s$ (scattering problem).

Next, we consider the scattering problem when a point acoustic source is generated at $x_0 = (10\,\text{mm}, 0, 0)$ and takes the form of $g(x,t) = 10f(t)\delta(x - x_0)$ (Figure 15, right). Again, $f(t)$ is the short Ricker pulse as shown in Figure 16. Let us denote p^{inc} as the pressure field in the absence of the elastic solid when the point source above is excited. It can be shown that $p^{inc}(x,t) = \frac{5}{2\pi|x|} f\left(t - \frac{|x|}{c}\right)$. We define the scattered pressure field as $p^s = p - p^{inc}$.

Note that the arrival time from the location of the sound source to the boundary of the elastic solid at $x_3 = 0$ is approximately $4.5\ \mu$s. The first three plots in Figure 19 are the scattered pressure field p^s on the plane $x_2 = 0$ when the first trough, the crest, and the second trough of the short pulse hits the boundary of the elastic structure, respectively, that is, for $t = 12.5$, 16.5, and $20.5\ \mu$s, respectively. The last plot in Figure 19 is the scattered pressure field p^s after multiple reflections in the acoustic–structure interaction system. Finally, the scattered pressure field at the locations of $(-5\,\text{mm}, 0, 0)$ and$(5\,\text{mm}, 0, 0)$ for $0 < t \leqslant 100\,\mu$s in shown in Figure 20.

6. CONCLUSION

A fast and high-order numerical method is presented for the transient analysis of acoustic–structure interactions in three dimensions. The exponential window technique is employed to add an artificial damping to the system so that a long duration for trailing zeroes is not necessary in the frequency-domain approach. To sample the physical quantities at a sequence of complex frequencies

DOI: 10.1002/nme

in an efficient way, a fast and accurate boundary integral equation solver with a computational cost of $O\left(N_\Gamma^{4/3}\log N_\Gamma\right)$ for each matrix-vector product is introduced. The accelerated algorithm is significantly more efficient than the non-accelerated one and is capable of dealing with the acoustic–structure interaction problem at medium or high frequencies within a reasonable time. Numerical studies are also presented to test the efficiency of the method and the accuracy of the obtained solutions.

APPENDIX A: SINGULAR PART OF THE ELASTIC GREEN TENSOR

For an elastic medium with wave numbers κ_p and κ_s for P-wave and S-wave, respectively, each component of the traction Green tensor $\mathbb{T}$ can be written explicitly as

$$T_{ij} = \frac{1}{2\pi r^2}\left\{(A_1 r_i r_j + A_2\delta_{ij})r_m n_m^{(y)} + \left(A_2 r_j n_i^{(y)} + A_3 r_i n_j^{(y)}\right)\right\},$$

where

$$r = |y-x|, r_j = \frac{y_j - x_j}{r}, \tau = \mathrm{i}\kappa_s r, \alpha = \frac{\kappa_p}{\kappa_s},$$

$$M(\tau) = \frac{e^{\alpha\tau}(1-\alpha\tau) - e^{\tau}(1-\tau)}{\tau^2}, \psi = e^{\tau} - M(\tau), \chi = e^{\alpha\tau}\alpha^2 - e^{\tau} + 3M(\tau),$$

and

$$\begin{aligned} A_1 &= \tau\chi'(\tau) - 3\chi, \\ A_2 &= (\tau\psi'(\tau) - \psi + \chi)/2, \\ A_3 &= \chi + (1/(2\alpha^2) - 1)(A_1 + 2A_2 + 3\chi). \end{aligned}$$

Note that

$$\tilde{\mathbf{W}}(\rho,\theta) = \mathbb{T}\boldsymbol{\psi} J v\rho,$$

where $\boldsymbol{\psi}$ is the density, v is the function that localizes the singularity, and J is the Jacobian. To obtain the expression for $\tilde{\mathbf{W}}_{-1}(\theta)$, the Taylor expansion of $y_j - x_j$ is needed:

$$\begin{aligned} y_j - x_j &= \rho\left[\frac{\partial y_j}{\partial u}(u_0,v_0)\cos\theta + \frac{\partial y_j}{\partial v}(u_0,v_0)\sin\theta\right] \\ &\quad + \rho^2\left[\frac{\partial^2 y_j}{\partial u^2}(u_0,v_0)\frac{\cos^2\theta}{2} + \frac{\partial^2 y_j}{\partial u\partial v}(u_0,v_0)\cos\theta\sin\theta + \frac{\partial y_j}{\partial v^2}(u_0,v_0)\frac{\sin^2\theta}{2}\right] + O(\rho^3) \\ &= \rho C_j(\theta) + \rho^2 D_j(\theta) + O(\rho^3), \end{aligned} \tag{A.1}$$

where we have introduced notations $C_j(\theta)$ and $D_j(\theta)$ for conciseness. Similarly,

$$r = \rho C(\theta)\left(1 + \rho\frac{E(\theta)}{C^2(\theta)}\right) + O(\rho^3). \tag{A.2}$$

In the aforementioned formula, $C(\theta) = \left(\sum_{j=1}^3 C_j^2(\theta)\right)^{1/2}$, and $E(\theta) = \sum_{j=1}^3 C_j(\theta)D_j(\theta)$. By combining (A.3) and (A.2), it follows that

$$\begin{aligned} \frac{y_j - x_j}{r} &= \frac{C_j}{C} + \rho\left(\frac{D_j}{C} - \frac{C_j E}{C^3}\right) + O(\rho^2) \\ &= d_{j,0} + \rho d_{j,1} + O(\rho^2). \end{aligned} \tag{A.3}$$

DOI: 10.1002/nme

Let $J_k = Jn_k$, where n_k is the kth component of the unit normal vector n, and using the aforementioned Taylor expansions, it follows that

$$\begin{aligned} T_{ij}J\rho &= \frac{1}{2\pi r^2}\left\{(A_1 r_i r_j + A_2\delta_{ij})r_m n_m^{(y)} + A_2 r_j n_i^{(y)} + A_3 r_i n_j^{(y)}\right\} J\rho \\ &= \frac{1}{2\pi r^2}\left\{(A_1 r_i r_j + A_2\delta_{ij})r_m J_m^{(y)} + A_2 r_j J_i^{(y)} + A_3 r_i J_j^{(y)}\right\}\rho \\ &= \frac{1}{2\pi}\left(\frac{1}{C^2\rho} + O(1)\right)\left\{\left(A_1\frac{C_iC_j}{C^2} + A_2\delta_{ij}\right)\frac{C_m}{C}J_m^{(y)}\right. \\ &\quad \left. + A_2\frac{C_j}{C}J_i^{(y)} + A_3\frac{C_i}{C}J_j^{(y)} + O(\rho)\right\}. \end{aligned}$$

The smooth terms in the aforementioned formula can be expanded as

$$J_k = J_{k,0} + \rho J_{k,1} + O(\rho^2), \tag{A.4}$$

$$A_j = A_{j,0} + \rho A_{j,1} + O(\rho^2) \quad (j = 1, 2, 3). \tag{A.5}$$

Therefore,

$$\begin{aligned} T_{ij}J\rho = \frac{1}{2\pi}\left(\frac{1}{C^2\rho} + O(1)\right)&\left\{\left(A_{1,0}\frac{C_iC_j}{C^2} + A_{2,0}\delta_{ij}\right)\frac{C_m}{C}J_{m,0}^{(y)}\right. \\ &\left. + A_{2,0}\frac{C_j}{C}J_{i,0}^{(y)} + A_{3,0}\frac{C_i}{C}J_{j,0}^{(y)} + O(\rho)\right\}. \end{aligned} \tag{A.6}$$

Finally, v and each component of $\boldsymbol{\psi}$ also admit smooth expansions:

$$v = 1 + O(\rho^2), \tag{A.7}$$

$$\psi_j = \psi_{j,0} + \rho\psi_{j,1} + O(\rho^2). \tag{A.8}$$

By combining (A.3)–(A.8), we obtain each component of $\tilde{\mathbf{W}}_{-1}$ as follows:

$$\begin{aligned} \tilde{W}_{-1,i}(\theta) &= \sum_{j=1}^{3}\frac{\psi_{j,0}}{2\pi C^2}\left\{\left(A_{1,0}\frac{C_iC_j}{C^2} + A_{2,0}\delta_{ij}\right)\frac{C_m}{C}J_{m,0}\right. \\ &\qquad \left. + A_{2,0}\frac{C_j}{C}J_{i,0} + A_{3,0}\frac{C_i}{C}J_{j,0}\right\} \\ &= \sum_{j=1}^{3}\frac{\psi_{j,0}}{2\pi C^2}\left\{A_{2,0}\frac{C_j}{C}J_{i,0} + A_{3,0}\frac{C_i}{C}J_{j,0}\right\} \quad (i = 1, 2, 3), \end{aligned}$$

where the last equality follows from the fact that $C_m J_{m,0} = 0$. By noting that $C_j(\theta) = -C_j(\theta+\pi)$, we also have $\tilde{\mathbf{W}}_{-1}(\theta) = -\tilde{\mathbf{W}}_{-1}(\theta + \pi)$.

APPENDIX B: ANALYTICAL SOLUTION FOR THE ACOUSTIC–STRUCTURE INTERACTION WITH A SPHERICAL INTERFACE

We derive the analytical solution for the frequency-domain problem (3.2)–(3.5) when Ω is a unit ball centered at origin. Both radiation and scattering problems are considered. In the following, r, θ, and φ are the radius, polar angle, and azimuthal angle, respectively.

DOI: 10.1002/nme

APPENDIX B.1 RADIATION PROBLEM

Consider the radiation problem with $\hat{\mathbf{f}} = \nabla\delta$. We split $\hat{\mathbf{u}}$ as $\hat{\mathbf{u}} = \hat{\mathbf{u}}_0 + \hat{\mathbf{u}}_1$, where

$$(\lambda + 2\mu)\ \nabla\nabla\cdot\hat{\mathbf{u}}_0 - \mu\ \nabla\times\nabla\times\hat{\mathbf{u}}_0 + \rho_e\omega^2\hat{\mathbf{u}}_0 = -\nabla\delta$$

and

$$(\lambda + 2\mu)\ \nabla\nabla\cdot\hat{\mathbf{u}}_1 - \mu\ \nabla\times\nabla\times\hat{\mathbf{u}}_1 + \rho_e\omega^2\hat{\mathbf{u}}_1 = 0.$$

Define $\psi_0 = \frac{1}{4\pi(\lambda+2\mu)r}e^{i\kappa_p r}$. It follows from a direct calculation that $\hat{\mathbf{u}}_0 = -\nabla\psi_0$ is a desired solution. $\hat{\mathbf{u}}_1$ is spherically symmetry and can be expressed as $\hat{\mathbf{u}}_1 = -\nabla\psi_1$, where $\psi_1 = c\ j_0(\kappa_p r)$ solves $\Delta\psi_1 + \kappa^2\psi_1 = 0$, j_0 is the spherical Bessel function and c_0 is the coefficient to be determined. Let $\psi = \psi_0 + \psi_1$. Then $\hat{\mathbf{u}} = -\nabla\psi$, and the three components of the displacement vector in the directions of increasing r, θ, and φ are

$$u_r = -\frac{\partial\psi}{\partial r} = -\frac{1}{4\pi(\lambda+2\mu)r}e^{i\kappa_p r}\left(i\kappa_p - \frac{1}{r}\right) - c\kappa_p j_0'(\kappa_p r), \quad u_\theta = 0, \quad \text{and } u_\varphi = 0. \tag{B.1}$$

On the other hand, the stress components acting on spherical surface in the directions of increasing r, θ, and φ are given by (cf. [52])

$$\begin{aligned}\sigma_r &= \rho_e\omega^2\left(\psi + \frac{4}{\kappa_s^2 r}\frac{\partial\psi}{\partial r}\right),\\ \sigma_\theta &= 0,\\ \sigma_\varphi &= 0.\end{aligned}$$

More explicitly,

$$\sigma_r = \frac{\rho_e\omega^2 e^{i\kappa_p r}}{4\pi(\lambda+2\mu)r}\left(1 + \frac{4}{\kappa_s^2 r}\left(i\kappa_p - \frac{1}{r}\right)\right) + c\ \rho_e\omega^2\left(j_0(\kappa_p r) + \frac{4}{\kappa_s^2 r}\kappa_p j_0'(\kappa_p r)\right). \tag{B.2}$$

Similarly, the pressure field in the exterior domain can be expressed as

$$p = d\ h_0^1(\kappa_f r), \tag{B.3}$$

where h_0^1 is the spherical Hankel function of the first kind and d is the coefficient to be determined. The continuity conditions (3.4) imply that $\sigma_r = -p$ and $\frac{\partial p}{\partial r} = \rho_f\omega^2 u_r$ for $r = 1$, and the unknown coefficients c and d can be determined by substituting (B.1)–(B.3) into these two equations.

APPENDIX B.2 SCATTERING PROBLEM

Consider the scattering problem when an incident wave $\hat{p}^{inc} = e^{-i\kappa_f x_3}$ impinges upon a homogeneous elastic ball. First, the incident wave adopts the so-called Jacobi–Anger expansion:

$$e^{-i\kappa_f x_3} = \sum_{m=0}^{\infty}(-i)^m(2m+1)\,j_m(\kappa_f r)\,P_m(\cos\theta), \tag{B.4}$$

where j_m is the spherical Bessel function and P_m is the Legendre polynomial. Because of the spherical symmetry, the scattered field p^s in the exterior acoustic medium can be expressed as

$$p^s = \sum_{m=0}^{\infty} a_m h_m(\kappa_p r)\,P_m(\cos\theta), \tag{B.5}$$

where h_m is the spherical Hankel function. Inside the solid, the displacement can be decomposed as $\hat{\mathbf{u}} = -\nabla\Psi + \nabla\nabla\cdot(\Phi\mathbf{r})$, where

DOI: 10.1002/nme

$$\Delta\Psi + \kappa_p^2\Psi = 0 \quad \text{and} \quad \Delta\Phi + \kappa_s^2\Phi = 0.$$

It follows that Ψ and Φ adopt the following expansions:

$$\Psi = \sum_{m=0}^{\infty} b_m j_m(\kappa_p r) P_m(\cos\theta) \quad \text{and} \quad \Phi = \sum_{m=0}^{\infty} c_m j_m(\kappa_s r) P_m(\cos\theta). \tag{B.6}$$

A direct calculation yields (cf. [52])

$$u_r = -\frac{\partial\Psi}{\partial r} - \frac{1}{r}Q(\Phi), \quad u_\theta = -\frac{1}{r}\frac{\partial\Psi}{\partial\theta} + \frac{1}{r}\frac{\partial^2(r\Phi)}{\partial\theta\partial r}, \quad u_\varphi = 0, \tag{B.7}$$

and

$$\begin{aligned}
\sigma_r &= \rho_e\omega^2\left(\Psi + \frac{2}{\kappa_s^2}\left[\frac{2}{r}\frac{\partial\psi}{\partial r} + \frac{1}{r^2}Q(\Psi) - \frac{\partial}{\partial r}\frac{Q(\Phi)}{r}\right]\right),\\
\sigma_\theta &= -2\frac{\rho_e\omega^2}{\kappa_s^2}\frac{\partial}{\partial\theta}\left(\frac{1}{r}\frac{\partial\Psi}{\partial r} - \frac{\Psi}{r^2} + \frac{1}{r}\frac{\partial\Phi}{\partial r} + \frac{1+\kappa_s^2 r^2/2}{r^2}\Phi + \frac{Q(\Psi)}{r^2}\right),\\
\sigma_\varphi &= 0.
\end{aligned} \tag{B.8}$$

Here, the operator $Q = \frac{1}{\sin\theta}\frac{\partial}{\partial\theta}\left(\sin\theta\frac{\partial}{\partial\theta}\right)$. By substituting the expansions (B.6) into (B.7) and (B.8), using the expansions (B.4) and (B.5) and applying the continuity conditions

$$\sigma_r = -(p^{inc} + p^s), \quad \sigma_\theta = 0, \quad \rho_f\omega^2 u_r = \frac{\partial}{\partial r}(p^{inc} + p^s)$$

over the acoustic–structure interface, we obtain the coefficients a_m, b_m, and c_m.

ACKNOWLEDGEMENTS

We thank Professor Mostafa Fatemi at Mayo Clinic for directing our attention to the problem presented in Example 3 of Section 5 and for interesting discussions. We also thank the anonymous referees for suggestions on improving the manuscript. This research is partially supported by the NSF grant DMS-1417676.

REFERENCES

1. Fatemi M, Greenleaf J. Ultrasound-stimulated vibro-acoustic spectrography. *Science* 1998; **280**:82–85.
2. Fahy F, Gardonio P. *Sound and Structural Vibration: Radiation, Transmission and Response*. Academic Press: Cambridge, 2007.
3. Morand M, Ohayon R. *Fluid Structure Interaction: Applied Numerical Methods*. John Wiley & Sons: Paris etc., Masson, 1995.
4. Ohayon R, Soize C. *Structural Acoustics and Vibration: Mechanical Models Variational Formulations and Discretization*. Elsevier, 1997.
5. Hsiao G, Kleinman R, Roach G. Weak solutions of fluid–solid interaction problems. *Mathematische Nachrichten* 2000; **218**:139–163.
6. Luke C, Martin P. Fluid–solid interaction: acoustic scattering by a smooth elastic obstacle. *SIAM Journal on Applied Mathematics* 1995; **55**:904–922.
7. Bielak J, MacCamy R. *Symmetric Finite Element and Boundary Integral Coupling Methods for Fluid–Solid Interaction*. Carnegie Mellon University: Technical Report, 1990.
8. Brunner D, Junge M, Gaul L. A comparison of FE–BE coupling schemes for large-scale problems with fluid–structure interaction. *International Journal for Numerical Methods in Engineering* 2009; **77**:664–688.
9. Everstine G. Finite element formulations of structural acoustics problems. *Computers and Structures* 1997; **6**: 307–321.
10. Everstine G, Henderson F. Coupled finite element/boundary element approach for fluid–structure interaction. *Journal of Acoustic Society of America* 1990; **87**:1938–1947.
11. Fischer M, Gaul L. Fast BEM–FEM mortar coupling for acoustic–structure interaction. *International Journal for Numerical Methods in Engineering* 2005; **62**:1677–1690.
12. Gatica G, Heuer N, Meddahi S. Coupling of mixed finite element and stabilized boundary element methods for a fluid–solid interaction problem in 3D. *Numerical Methods for Partial Differential Equations* 2014; **30**:1211–1233.
13. Li J et al. A dual-primal FETI method for solving a class of fluid–structure interaction problems in the frequency domain. *International Journal for Numerical Methods in Engineering* 2012; **89**:418–437.

DOI: 10.1002/nme

14. Mariem B, Hamdi M. A new boundary finite element method for fluid–structure interaction problems. *International Journal for Numerical Methods in Engineering* 1987; **24**:1251–1267.
15. Márquez A, Meddahi S, Selgas V. A new BEM–FEM coupling strategy for two-dimensional fluid–solid interaction problems. *Journal of Computational Physics* 2004; **199**:205–220.
16. Olson L, Bathe K. An infinite element for analysis of transient fluid–structure interactions. *Engineering Computations* 1985; **2**:319–329.
17. Rajakumar C, Ali A. Boundary element-finite element coupled eigenanalysis of fluid–structure systems. *International Journal for Numerical Methods in Engineering* 1996; **39**:1625–1634.
18. Tezaur R, Zhang L, Farhat C. A discontinuous enrichment method for capturing evanescent waves in multiscale fluid and fluid/solid problems. *Computer Methods in Applied Mechanics and Engineering* 2008; **197**:1680–1698.
19. Schneider S. FE/FMBE coupling to model fluid–structure interaction. *International Journal for Numerical Methods in Engineering* 2008; **76**:2137–2156.
20. Seybert A, Wu T, Wu X. Radiation and scattering of acoustic waves from elastic solids and shells using the boundary element method. *Journal of Acoustic Society of America* 1988; **84**:1906–1912.
21. Soares D, Godinho L. An optimized BEM–FEM iterative coupling algorithm for acoustic–elastodynamic interaction analyses in the frequency domain. *Computers and Structures* 2012; **106**:68–80.
22. Wilkes D, Duncan A. Acoustic coupled fluid–structure interactions using a unified fast multipole boundary element method. *Journal of Acoustic Society of America* 2015; **137**:2158–2167.
23. Wilton D. Acoustic radiation and scattering from elastic structures. *International Journal for Numerical Methods in Engineering* 1978; **13**:123–138.
24. Komatitsch D, Barnes C, Tromp J. Wave propagation near a fluid–solid interface: a spectral-element approach. *Geophysics* 2000; **65**:623–631.
25. Pinsky P, Abboud N. Transient finite element analysis of the exterior structural acoustics problem. *Journal of Vibration and Acoustics* 1990; **112**:245–256.
26. Sprague M, Geers TL. A spectral-element method for modelling cavitation in transient fluid–structure interaction. *International Journal for Numerical Methods in Engineering* 2004; **60**:2467–2499.
27. Thompson L, Pinsky P. A space–time finite element method for structural acoustics in infinite domains part 1: formulation, stability and convergence. *Computer Methods in Applied Mechanics and Engineering* 1996; **132**: 195–227.
28. Wang X, Bathe K. Displacement/pressure based mixed finite element formulations for acoustic fluid–structure interaction problems. *International Journal for Numerical Methods in Engineering* 1997; **40**:2001–2017.
29. Engquist B, Majda A. Absorbing boundary conditions for the numerical simulation of waves. *Mathematics of Computation* 1977; **31**:629–651.
30. Berenger J. A perfectly matched layer for the absorption of electromagnetic waves. *Journal of Computational Physics* 1994; **114**:185–200.
31. Diaz J, Joly P. A time domain analysis of PML models in acoustics. *Computer Methods in Applied Mechanics and Engineering* 2006; **195**:3820–3853.
32. Chen Z, Wu X. Long-time stability and convergence of the uniaxial perfectly matched layer method for time-domain acoustic scattering problems. *SIAM Journal on Numerical Analysis* 2012; **50**:2632–2655.
33. Estorff O, Antes H. On FEM–BEM coupling for fluid–structure interaction analyses in the time domain. *International Journal for Numerical Methods in Engineering* 1991; **31**:1151–1168.
34. Kallivokas L, Bielak J. Time-domain analysis of transient structural acoustics problems based on the finite element method and a novel absorbing boundary element. *Journal of Acoustic Society of America* 1993; **94**:3480–3492.
35. Banjai L, Schanz M. Wave propagation problems treated with convolution quadrature and BEM. *Fast Boundary Element Methods in Engineering and Industrial Applications*, Springer, Berlin Heidelberg, 2012; 145–184.
36. Coifman R, Rokhlin V, Wandzura S. The fast multipole method for the wave equation: a pedestrian prescription. *IEEE Antennas and Propagation Magazine* 1993; **35**:7–12.
37. Nishimura N. Fast multipole accelerated boundary integral equation methods. *Applied Mechanics Review* 2002; **55**:299–324.
38. Rokhlin V. Diagonal form of translation operators for the Helmholtz equation in three dimensions. *Applied and Computational Harmonic Analysis* 1993; **1**:82–93.
39. Canino L, Ottusch J, Stalzer M, Visher J, Wandzura S. Numerical solution of the Helmholtz equation using a high-order Nystrom discretization. *Journal of Computational Physics* 1998; **146**:627–663.
40. Song J, Lu C, Chew W, Lee S. Fast Illinois solver code (FISC). *IEEE Antennas and Propagation Magazine* 1998; **40**:27–34.
41. Tong M, Chew W. Multilevel fast multipole algorithm for elastic wave scattering by large three-dimensional objects. *Journal of Computational Physcis* 2009; **228**:921–932.
42. Kausel E, Roësset J. Frequency domain analysis of undamped systems. *Journal of Engineering Mechanics* 1992; **118**:721–734.
43. Phan A et al. Frequency domain analysis by the exponential window method and SGBEM for elastodynamics. *Computational Mechanics* 2011; **48**:615–630.
44. Xiao J, et al. Precorrected FFT accelerated BEM for large scale transient elastodynamic analysis using frequency-domain approach. *International Journal for Numerical Methods in Engineering* 2012; **90**:116–134.
45. Bruno O, Kunyansky L. A fast, high-order algorithm for the solution of surface scattering problems: basic implementation, tests and applications. *Journal of Computational Physics* 2001; **169**:80–110.

DOI: 10.1002/nme

46. Bu F, Lin J, Reitich F. A fast and high-order method for the three-dimensional elastic wave scattering problem. *Journal of Computational Physics* 2014; **258**:856–870.
47. Pao YH, Varatharajulu V. Huygens' principle, radiation conditions, and integral formulas for the scattering of elastic waves. *Journal of Acoustic Society of America* 1976; **59**:1361–1371.
48. Saad Y, Schultz MH. GMRESA: a generalized minimal residual algorithm for solving non-symmetric linear systems. *SIAM Journal on Scientific and Statistical Computing* 1986; **7**:856–869.
49. Adams R, Fournier J. *Sobolev Spaces, Chapter 2. Pure and Applied Mathematics*, Vol. 140. Academic Press: Oxford, 2003.
50. Aki A, Richards PG. *Quantitative Seismology*, (2 ed.) University Science Books: Sausalito, California, 2002.
51. Felsen L, Marcuvitz N. *Radiation and Scattering of Waves*. Printice Hall: Englewood Cliffs, New Jersey, 1973.
52. Ying C, Truell R. Scattering of a plane longitudinal wave by a spherical obstacle in an isotropically elastic solid. *Journal of Applied Physics* 1956; **27**:1086–1097.

DOI: 10.1002/nme